AGU PUBLICATIONS

Geochemistry, Geophysics, Geosystems

RESEARCH ARTICLE
10.1002/2014GC005693

Quantifying near-field and off-fault deformation patterns of the 1992 M_w 7.3 Landers earthquake

Christopher W. D. Milliner[1], James F. Dolan[1], James Hollingsworth[2], Sebastien Leprince[3], Francois Ayoub[3], and Charles G. Sammis[1]

[1]Department of Earth Sciences, University of Southern California, Los Angeles, California, USA, [2]Arup, London, UK, [3]Division of Geological and Planetary Sciences, California Institute of Technology, Pasadena, California, USA

Key Points:
- We measure the near-field, surface deformation pattern of the Landers event
- We measure the fault displacement, deformation width, and off-fault deformation
- Slip is found to be fractal, which has implications for earthquake behavior

Supporting Information:
- Supporting Information S1

Correspondence to:
C. W. D. Milliner,
milliner@usc.edu

Citation:
Milliner, C. W. D., J. F. Dolan, J. Hollingsworth, S. Leprince, F. Ayoub, and C. G. Sammis (2015), Quantifying near-field and off-fault deformation patterns of the 1992 M_w 7.3 Landers earthquake, *Geochem. Geophys. Geosyst.*, *16*, 1577–1598, doi:10.1002/2014GC005693.

Received 15 DEC 2014
Accepted 30 MAR 2015
Accepted article online 7 APR 2015
Published online 27 MAY 2015

Abstract Coseismic surface deformation in large earthquakes is typically measured using field mapping and with a range of geodetic methods (e.g., InSAR, lidar differencing, and GPS). Current methods, however, either fail to capture patterns of near-field coseismic surface deformation or lack preevent data. Consequently, the characteristics of off-fault deformation and the parameters that control it remain poorly understood. We develop a standardized method to fully measure the surface, near-field, coseismic deformation patterns at high resolution using the COSI-Corr program by correlating pairs of aerial photographs taken before and after the 1992 M_w 7.3 Landers earthquake. COSI-Corr offers the advantage of measuring displacement across the entire zone of surface deformation and over a wider aperture than that available to field geologists. For the Landers earthquake, our measured displacements are systematically larger than the field measurements, indicating the presence of off-fault deformation. We show that 46% of the total surface displacement occurred as off-fault deformation, over a mean deformation width of 154 m. The magnitude and width of off-fault deformation along the rupture is primarily controlled by the macroscopic structural complexity of the fault system, with a weak correlation with the type of near-surface materials through which the rupture propagated. Both the magnitude and width of distributed deformation are largest in stepovers, bends, and at the southern termination of the surface rupture. We find that slip along the surface rupture exhibits a consistent degree of variability at all observable length scales and that the slip distribution is self-affine fractal with dimension of 1.56.

1. Introduction

Large-magnitude strike-slip earthquakes that rupture to the surface are an important source of information for finite-fault inversions and studies of faulting mechanics. In particular, the extent to which coseismic fault slip is localized or distributed in the near-surface gives insight into the initiation, propagation, and cessation of dynamic ruptures, the structural evolution of faults, the use of surface slip data in probabilistic seismic hazard assessment (PSHA), the measurement of geologic fault slip rates, and comparison of these data to geodetic rates [*Sammis et al.*, 2009; *Shelef and Oskin*, 2010; *Chen and Petersen*, 2011; *Petersen et al.*, 2011; *Johnson et al.*, 1994; *Dolan and Haravitch*, 2014; *Herbert et al.*, 2014]. Constraining the width of the deformation zone and lateral variations of on and off-fault displacement may provide predictive information on the locations of the likely endpoints of future ruptures [e.g., *Wesnousky*, 2006, 2008; *Elliott et al.*, 2009; *Rockwell and Klinger*, 2013].

Surface deformation along coseismic ruptures typically releases the accumulated interseismic strain energy as a combination of slip along discrete, brittle faults and off-fault, inelastic deformation expressed physically as warping, granular flow, rigid-block rotation, minor secondary faulting, and/or microcracking. Observations of surface deformation patterns from numerous strike-slip faults demonstrate that the magnitude of off-fault deformation (OFD) can vary from 0 to 100% [e.g., *Nelson and Jones*, 1987; *Miller and Yount*, 2002; *Rockwell et al.*, 2002; *Treiman et al.*, 2002; *Kimurah et al.*, 2004; *Shelef and Oskin*, 2010; *Van Dissen et al.*, 2011; *Quigley et al.*, 2012] and has been observed to vary systematically according to the structural maturity of the fault [*Milliner et al.*, 2012; *Dolan and Haravitch*, 2014]. Compliant zones of reduced shear rigidity surrounding many fault zones are a manifestation of OFD mechanisms damaging

the rock over the entire history of deformation [e.g., *Li et al*., 1998; *Vermilye and Scholz*, 1998; *Chester and Chester*, 1998; *Yamashita*, 2000; *Ben-Zion et al*., 2003; *Mamada et al*., 2004; *Chester et al*., 2005; *Lemaitre and Desmorat*, 2005; *McGuire and Ben-Zion*, 2005; *Cochran et al*., 2009; *Frost et al*., 2009; *Shelef and Oskin*, 2010]. These compliant zones are well observed using geodetic and seismic data with widths measured up to ~2 km [e.g., *Fialko et al*., 2002; *Cochran et al*., 2009]. Similar deformation widths are also found from geologic studies that measure distributed shear accommodated over geologic time scales. For example, *Oskin et al*. [2007] and *Shelef and Oskin* [2010] measured a ~2 km wide zone of distributed deformation for the Calico fault in the eastern California shear zone and noted that the majority of deformation was confined to a higher strain 100–200 m wide fault core. This narrower width is similar to the total observed width of distributed deformation in many surface ruptures [e.g., *McGill and Rubin*, 1999; *Treiman et al*., 2002; *Rockwell et al*., 2002; *Oskin et al*., 2012].

Although off-fault deformation has been observed along many faults, the controls of off-fault deformation along a coseismic surface rupture remain poorly understood. Moreover, although a number of different techniques have been utilized to document OFD patterns, there is as yet no standard method to robustly and reproducibly measure the characteristics of the complex, near-field surface deformation in high resolution with readily available and cost-effective data. For example, although Interferometric Synthetic Aperture Radar (InSAR) studies reveal the surface deformation field in exceptional detail, they typically decorrelate close to surface ruptures as deformation gradients exceed a single phase cycle between neighboring radar returns [e.g., *Burgmann et al*., 2000; *Simons et al*., 2002; *Cakir et al*., 2003; *Fialko*, 2004]. Field surveys can provide very precise measurements of on-fault deformation, but they do not typically account for more subtle, complex off-fault deformation, which can be challenging to measure [e.g., *McGill and Rubin*, 1999; *Treiman et al*., 2002; *Rockwell et al*., 2002; *Shelef and Oskin*, 2010; *Gold et al*., 2013]. GPS data, while providing exceptional temporal resolution, also lack the necessary spatial coverage to fully characterize the near-field deformation pattern. Lidar (light detection and ranging) data have proven to be a valuable tool in studies of near-field surface deformation [e.g., *Oskin et al*., 2012; *Nissen et al*., 2014], but acquisition of lidar data is costly and lidar differencing requires the existence of preexisting data, which is not always the case. Cross correlation of high-resolution, optical satellite imagery acquired before and after an earthquake can also reveal the first-order surface deformation patterns in earthquakes [*Leprince et al*., 2007a, 2007b, 2008; *Ayoub et al*., 2009; *Konca et al*., 2010; *Hollingsworth et al*., 2013]. However, the relatively coarse spatial resolution (typically >1 m) of most satellite data inhibit the detailed analysis of complex and sometimes subtle near-field deformation patterns.

In light of these limitations, the primary goal of this study is to further develop the methodology set out originally by *Michel and Avouac* [2006]; *Ayoub et al*. [2009] and *Hollingsworth et al*. [2012] for the use of cross correlation of high-resolution, pre and postevent aerial photographs to understand patterns of surface deformation. We tested this methodology through measurements of the near-field ground deformation from the M_w 7.3 1992 Landers earthquake. Such optical image correlation based on aerial photographs can facilitate measurement of the distributed inelastic strain, as this technique has the capability to capture the entire deformation across a fault [e.g., *Michel and Avouac*, 2006; *Konca et al*., 2010]. As part of our analysis, we used numerous statistical tests to understand whether off-fault deformation and the fault zone width vary according to any observable parameters that may facilitate the prediction of strain localization in advance of future large earthquakes. Finally, we discuss the implications of these results for studies of fault mechanics, the potential underestimation of slip rates, the dynamics of coseismic ruptures, and strategies to mitigate damage to the built environment.

1.1. M_w 7.3, 1992 Landers Earthquake

The Landers earthquake occurred within an 80 km wide zone of NNW-trending, right-lateral faults known as the eastern California shear zone, which accommodates ~25% of the total Pacific and North-American plate motion [*Humphreys and Weldon*, 1994; *Sauber et al*., 1994; *Dixon et al*., 2000; *Oskin et al*., 2008; *Frankel et al*., 2011]. The Landers earthquake was generated by rupture of five distinct faults over a distance of 67 km [*Bryant*, 1992, 1994; *Liu et al*., 2003] (Figure 1b). Rupture initiated near its southern end, on the Johnson Valley fault, and propagated unilaterally to the north-northwest across two right-stepping, dilational stepovers, before terminating along the Camp Rock fault [*Wald and Heaton*, 1994]. Detailed mapping of the Landers rupture by field geologists found particularly complex deformation patterns. For example, *McGill and Rubin* [1999] recorded significant variations in offset along 1–2 km stretches of the Emerson fault,

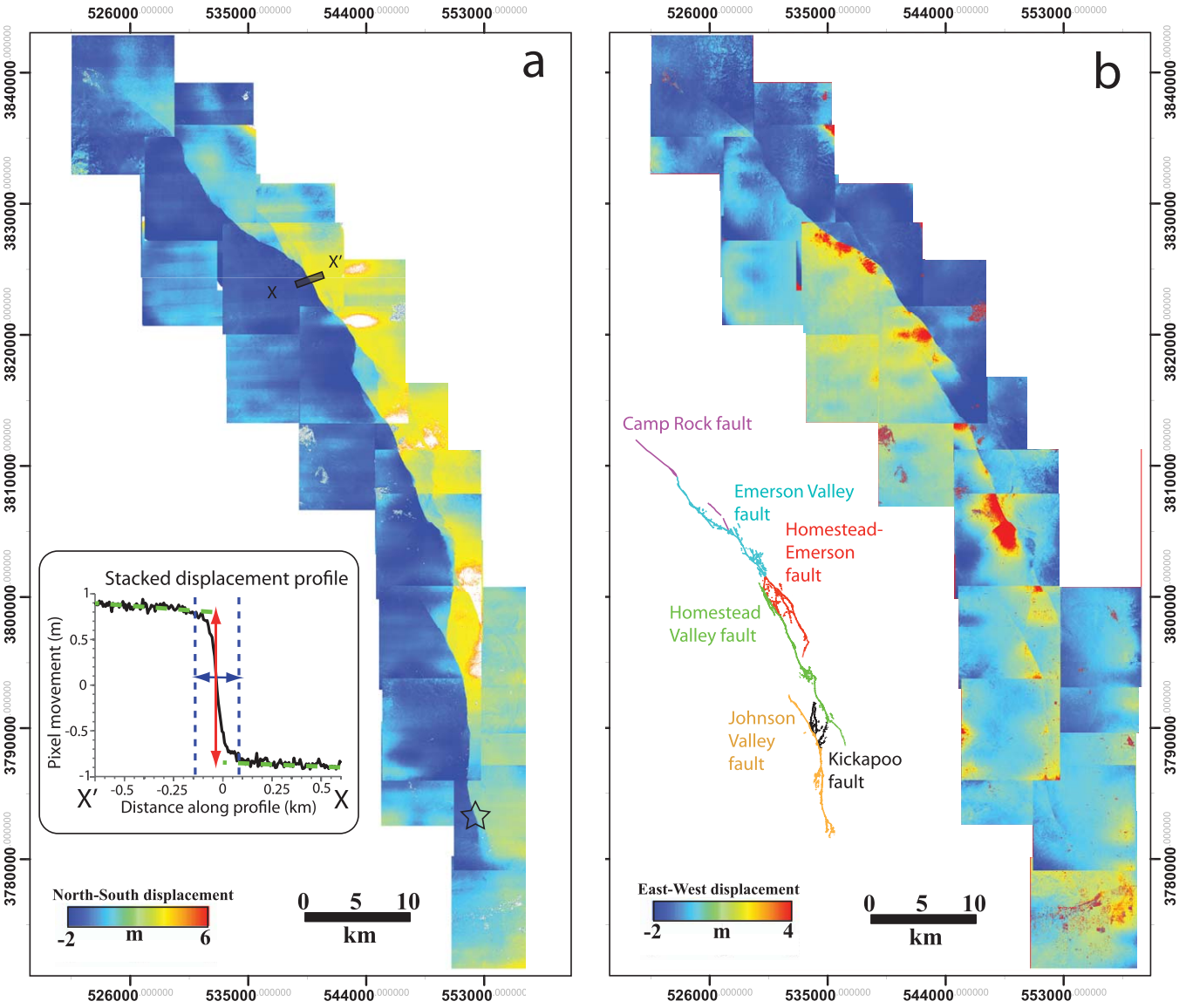

Figure 1. Correlation maps from 31 aerial image pairs which bracket the Landers earthquake. Black star shows location of 1992 M_w 7.3 epicenter with map coordinates in UTM. (a) North-south correlation map, positive pixel values indicates movement to the south and negative to the north. The lower left inset shows fault-parallel displacement within a 138 m wide stacked profile from X-X′ and illustrates how the displacement and fault zone width are measured. (b) East-west correlation result with positive pixel values indicating pixel movement to west and negative to the east. Inset fault map in lower left corner shows annotated Landers surface rupture [*Liu et al.*, 2003].

Spotila and Sieh [1995] documented areas of reduced slip (termed "slip gaps") along the Homestead Valley fault thought to be controlled by fault structural complexity, and *Zachariasen and Sieh* [1995] noted distributed, but efficient transfer of slip onto a series of right-stepping *en-echelon* faults within the Homestead-Emerson stepover. Although these field studies found instances of complex deformation patterns along the rupture, they could neither completely capture the magnitude nor the distribution of off-fault deformation along the entire surface rupture.

Postseismic deformation from the Landers earthquake included poroelastic rebound and up to 15 cm of afterslip at the surface as observed by geodetic surveys 7 years following the earthquake [*Peltzer et al.*, 1998; *Fialko*, 2004]. Slip rate estimates for the Camp Rock fault indicate $<1.4 \pm 0.6$ mm/yr of strain accommodated over the past 50 ± 20 ka [*Oskin et al.*, 2008], with analysis of basement offsets indicating a cumulative displacement of ~3.5 km for the faults that ruptured in the Landers event [*Jachens et al.*, 2002].

2. Observations

2.1. Cross Correlation of Optical Imagery

We used the COSI-Corr software (coregistration of optically sensed images and correlation) to correlate pairs of pre and postevent optical images with subpixel precision, in order to quantify the magnitude and distribution of near-field coseismic ground deformation [*Leprince et al*., 2007a; *Ayoub et al*., 2009]. This technique has been used successfully with satellite imagery to document surface deformation in earthquakes, landslides, glacier dynamics, and the migration of Martian sand dunes and dikes [*Avouac et al*., 2006; *Leprince et al*., 2008; *Bridges et al*., 2012; *Hollingsworth et al*., 2012]. Air photos offer the advantage of significantly greater pixel resolution (1 m) than the satellite data available before the 1992, Landers event, which allows us to quantify the near-field surface deformation pattern in unprecedented detail.

To produce correlation maps that accurately constrain the ground deformation pattern, the input aerial photographs must be precisely orthorectified (i.e., create a planimetric correct image where objects are in their true ground geometry) and coregistered before correlation. The COSI-Corr procedure allows for accurate orthorectification of images by taking into account the topography using a digital elevation model (DEM), the internal camera geometry using a camera calibration report to correct for optical distortions (such as radially increasing incidence angle from near-nadir at image center to $\sim 30^{\circ}$ at image edges), and the exterior orientation (look angle and altitude) determined from ground control points (GCPs) [*Ayoub et al*., 2009]. To coregister the pre and postevent photographs, we construct a relative mapping between image pairs using tie points that relate common features in the image scene. COSI-Corr then applies subpixel image correlation on the set of orthoimages by using an iterative, unbiased processor that estimates the phase plane in the Fourier domain [*Leprince et al*., 2007a, 2007b, 2008; *Ayoub et al*., 2009]. The correlation process yields two correlation maps, representing pixel motion in the east-west and north-south horizontal directions of the surface displacement field, with an accuracy of $1/10^{th}$ the size of the input image pixel dimension [*Ayoub et al*., 2009]. The aerial photographs have 1 m ground-resolution pixel size, which therefore allows detection of horizontal deformation down to an accuracy of $\sim$10 cm. This represents a minimum detection threshold in our correlation maps, and smaller surface displacements cannot be resolved with these data. Although our methodology does not constrain vertical deformation [see *Michel and Avouac*, 2006; *Hollingsworth et al*., 2012], the majority of the deformation in this predominantly strike-slip earthquake was horizontal [*Sieh et al*., 1993; *Bryant*, 1992, 1994; *Spotila and Sieh*, 1995; *Zachariasen and Sieh*, 1995; *McGill and Rubin*, 1999].

2.1.1. Data

We selected 31 pairs of panchromatic, 1 m resolution, National Aerial Photography Program (NAPP) aerial photographs for correlation, purchased from the USGS (http://earthexplorer.usgs.gov/). Stereo-pair (60% overlap) pre and postevent photos were acquired in July 1989 and May 1994, respectively, with 8×8 km footprints and were orthorectified using the same 2012, 10 m National Elevation Datum (NED), DEM from the USGS (http://ned.usgs.gov/). To georeference the postevent aerial photos (i.e., assign absolute ground coordinates), we used 2005, SPOT 5 satellite imagery as the reference orthoimage. To orthorectify the air photos, GCPs are assumed to have experienced zero-ground deformation; however, as they are collected near the surface rupture the presence of long-wavelength ground deformation violates this assumption. To correct for this we used a cross-correlation result from a pair of 10 m, SPOT 5 images, which provides independent information on the ground deformation [*Milliner et al*., 2012].

2.1.2. Optical Image Cross-Correlation Result

Our cross correlation of the optical aerial photographs from before (1989) and after (1994) the Landers earthquake reveals the detailed surface deformation field associated with the rupture (Figure 1). From multiple tests we determined the optimal correlation parameters (i.e., those that suppress noise and decorrelation but retains details of the surface rupture) were a multiscale sliding window of 64 to 32 pixels with a step of six pixels, which results in a correlation map of 6 m pixel resolution.

The output correlation maps are found to contain both tectonic and artificial signals. Such artifacts include scanning distortions from film digitization, radial distortions from unmodelled lens parameters, and film distortion due to thermomechanical warping of the original photographic film [*Ayoub et al*., 2009]. Using a series of synthetic tests (detailed in supporting information) we found the artificial signals occur at much longer wavelengths than the observed shorter-wavelength tectonic signals and do not bias our

measurements of surface displacement (see Figures S1–S3), in agreement with *Michel and Avouac* [2006]. Topographic artifacts in the correlation result caused by using only a single postevent DEM to orthorectify both the pre and postevent photos are corrected for following the procedure of *Ayoub et al*. [2009].

2.2. Measuring Coseismic Surface Displacement

We measured the total surface displacement across the entire width of deformation along the Landers surface rupture using stacked profiles orientated perpendicular to the fault strike. The profile lengths ranged from ~2 to 3 km (perpendicular to fault) and were stacked over a 138 m, along-strike length (i.e., the fault-parallel displacement is averaged over a 138 m fault-parallel distance). Thus, each measurement can be considered independent from each other, with a discretization determined by the stack width [*Michel and Avouac*, 2006; *Konca et al*., 2010]. Testing of different stack widths indicated an optimal width of 138 m, which allows for suppression of noise in the correlation maps while minimizing oversmoothing of along-strike changes in surface slip (Figure S4). Surface displacement is measured from the stacked profiles by manually fitting linear regressions to the deformation signal on either side of the fault, and the relative difference of the extrapolated regressions defines the magnitude of the offset accommodated across the entire fault zone (Figure 1a). Thus, the COSI-Corr "displacement" value includes both the localized, on-fault displacement that occurs on the primary fault strand, as well as any off-fault, distributed inelastic shear accommodated via a range of physical processes.

To reliably understand the slip behavior and detailed pattern of surface strain localization, we need to characterize any error that arises from subjectively measuring the displacement and fault zone width (FZW). Estimating the width of shear and magnitude of fault offset from the stacked profiles involves subjectively locating the sometimes subtle inflection point in the profile on either side of the fault (dashed blue lines in Figure 1a). To quantify the measurement precision and any possible bias in this procedure, we employed synthetic tests (detailed in supporting information), in which we synthetically sheared an image with known and constant FZW and displacement. Using COSI-Corr, we then cross-correlated the synthetically sheared image with another image of the same location, acquired at a different time (Figure S1). As the FZW and displacement were kept constant, any deviation from the synthetic, known values gives a direct quantification of the measurement bias and precision, which reflects measurement subjectivity and variation in image quality and texture. The synthetic tests reveal a bias of 0.01 m overestimation with a precision of $\pm$0.12 m (2σ) for our displacement measurements (Figure S3) and an underestimation of 2 m and precision of $\pm$11.70 m (2σ) for the FZW measurements (Figure S4). These values, which are independent of the magnitude of displacement and width of deformation, allow us to derive an empirical error distribution for the displacement and FZW measurements, which is then propagated through the preexisting error in our COSI-Corr results. Capturing and incorporating this variability is noteworthy given it usually forms a significant component of the epistemic uncertainty in most studies that measure coseismic displacement.

2.2.1. Landers Surface Displacements

In the correlation maps we detected 69 distinct fault segments that accommodated surface slip larger than our minimum detection threshold (>10 cm). These agree well with the locations of fault strands mapped in the field following the earthquake [*Bryant*, 1992, 1994; *Liu et al*., 2003, and references therein]. We collected a total of 1057 coseismic, surface displacement measurements spaced every 138 m along all of the mapped fault traces (Figure 2b) and found a maximum displacement of 5.58 $\pm$ 0.14 m (95% confidence interval of measurement precision) and a mean of 1.52 $\pm$ 0.70 m (1σ) and median of 1.00 m. Generally speaking, we found the highest displacements on structurally simple, single-stranded sections of the Landers rupture, such as the Homestead fault and parts of the central Emerson fault. Conversely, we found that coseismic slip decreases on individual faults in structurally complex areas (e.g., the Kickapoo and Homestead-Emerson stepovers), due to transfer of total surface slip onto multiple structures.

Our 1057 displacement measurements are distributed in a spatially complex manner along the rupture and therefore constructing a precise along-strike slip-profile of the 1992 Landers event is a nontrivial task. To overcome this, we developed an algorithm that projects all 1057 of our displacement measurements onto a single, regionally representative "fault trace." To collapse multiple faults onto a single, regionally representative "fault," we iteratively projected each individual fault strand sequentially, calculated the component of slip using a cubic interpolation and added this to eventually construct the cumulative slip distribution (thick, black line in Figure 3).

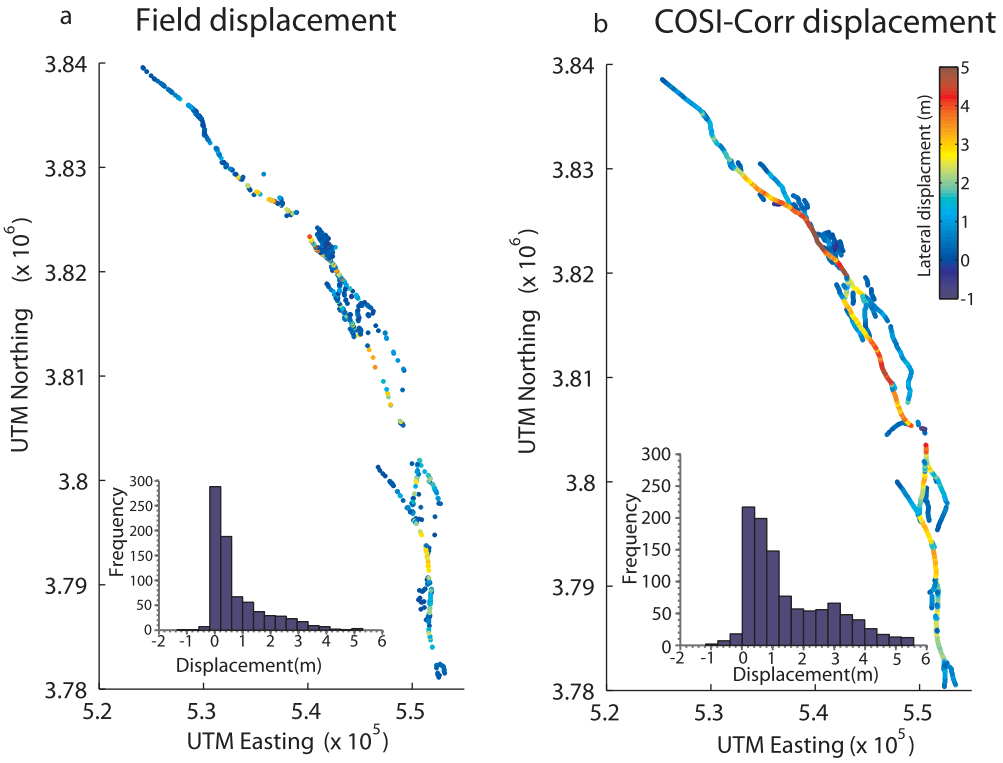

Figure 2. (a) Map view of field data compiled from *Liu et al*. [2003] and *Bryant* [1992, 1994] that are used to calculate off-fault deformation (OFD), positive values denote right-lateral displacement, negative left-lateral displacement. (b) Map view of all 1057 displacements measured from the correlation maps. Inset images in lower left corners of Figures 2a and 2b show histogram of data.

The position of the regional "fault" used here agrees well with the macroscopic, first-order geometry of the fault system that ruptured during the Landers earthquake [*Bryant*, 1992, 1994; *Liu et al*., 2003, and references therein] as well as the location of faults at depth used in the inversion of geodetic data [*Fialko*, 2004]. The projection of the displacement measurements also corrects for slip transfer between branching or parallel fault structures, which if left unaccounted for can lead to arbitrary along-strike slip variability. As our displacement measurements are spatially dense, incorporate OFD, and cover the entire Landers rupture, including secondary faults, once projected, the displacement data set yields a robust and systematically complete representation of the Landers slip distribution

Generally, the Landers slip profile has a simple, first-order shape, with two prominent peaks (labeled i and ii in Figure 3a) and two areas of significantly reduced slip ("slip gaps," labeled iii and iv), the latter likely related to the fault segmentation (which is discussed further in section 3.1) [*Spotila and Sieh*, 1995]. The COSI-Corr displacement measurements (which include OFD) exhibit pronounced short-wavelength, along-strike variation, which consistently occurs along all 69 fault segments (see Figure 3). The slip variation is as large as $\pm$0.5 m over along-strike distances of $\sim$200 m, which is significantly more than the measurement precision (95% confidence interval of $\pm$0.12 m, see supporting information Figure S4). As the observed along-strike slip variability cannot be accounted for by the measurement error, this suggests the slip heterogeneity reflects the true physical behavior of the faulting and is consistent with other studies that document coseismic slip along the Landers rupture [*McGill and Rubin*, 1999] and other surface ruptures [e.g., *Rockwell et al*., 2002; *Klinger et al*., 2006; *Rockwell and Klinger*, 2013].

The presence of along-strike slip variability produces along-strike strains, which are found to vary up to 2.0 $\times$ 10^{-3} over $\sim$200 m along-strike distances. Along-strike strain is calculated as the change in slip per unit distance along-strike and halved in order to determine deformation on either side of the fault. *McGill and Rubin* [1999] reported similar magnitudes of along-strike strain of $\sim 10^{-2}$ for the Landers surface displacement and similar strains of 10^{-3} have been documented for other earthquakes [e.g., *Michel and Avouac*, 2006; *Oglesby*, 2008; *Elliott et al*., 2009; *Oskin et al*., 2012; *Gold et al*., 2013].

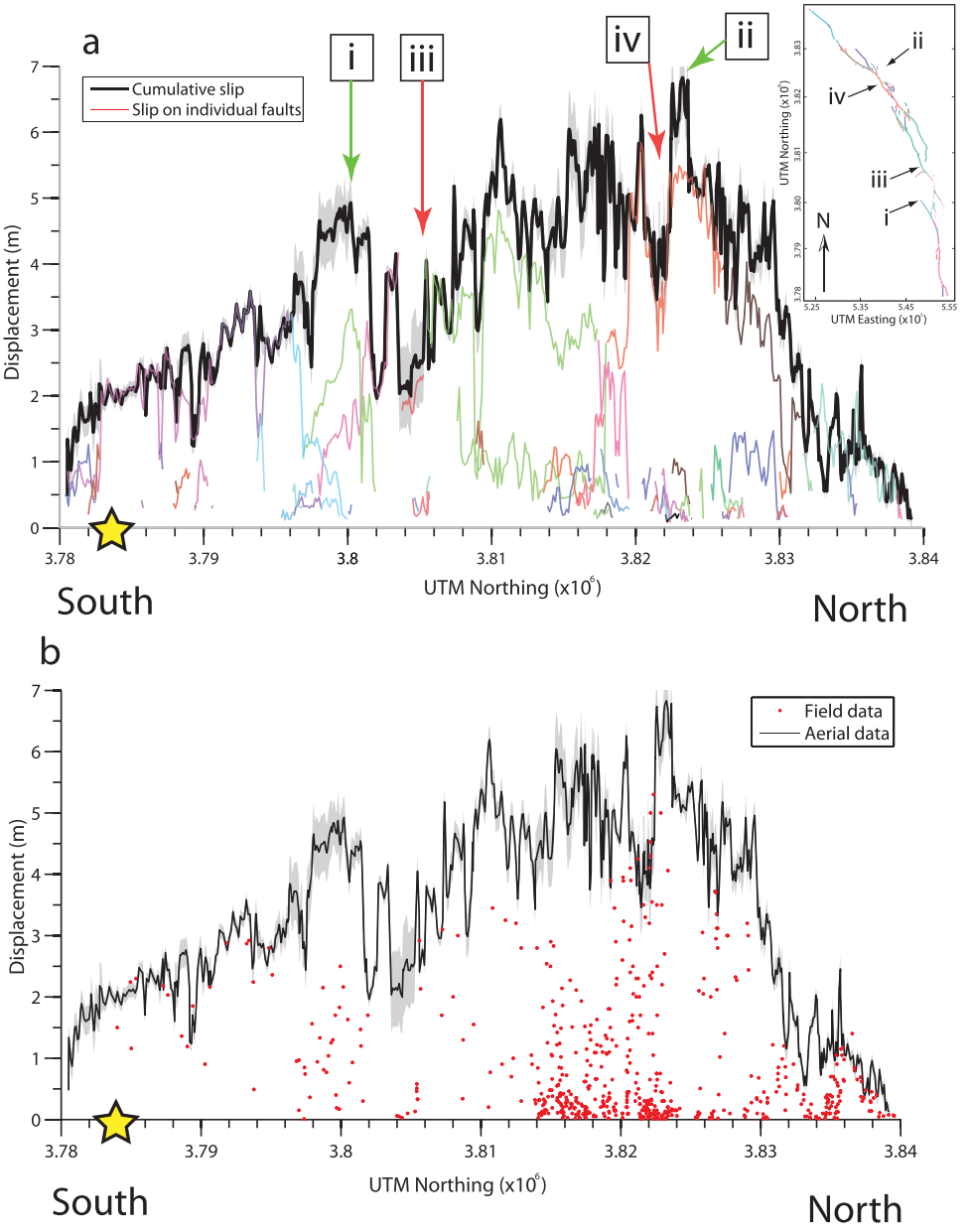

Figure 3. (a) Landers offset profile from our COSI-Corr displacement measurements plotted as a function of UTM Northing. Thin multicolored lines show the offset profiles for individual faults. Thick black line shows the projected, cumulative offset profile for Landers. Green colored arrows, labeled i and ii, indicate the major peaks of displacement and red colored arrows labeled iii and iv indicate the areas of reduced slip, termed "slip gaps" [*Spotila and Sieh*, 1995]. Yellow star denotes the location of the epicenter. Inset map in top right corner illustrates faults used in the slip profile with their corresponding colors used in the offset profile. (b) Cumulative, projected displacement (black line) plotted against UTM Northing, with the field displacement from *Bryant* [1992, 1994] and *Liu et al.* [2003, and references therein], plotted as red dots.

To understand if there is an underlying structure to the slip variability, and how the variability changes with frequency, we used a spectral analysis by computing the power spectrum $P(k)$ of the slip distribution (Figure 3) using the Thomson multitaper method [*Thomson*, 1982]. The spectral analysis reveals that the coseismic slip distribution follows a power-law decay (Figure 4); we use a linear regression to estimate a decay parameter β of 1.87 ± 0.04 (95% confidence interval), with an $R^2 = 0.80$. Following equation (2), β gives a fractal dimension D of 1.56 ± 0.04, indicating that the coseismic slip distribution is fractal and scale invariant (i.e., slip exhibits a statistically consistent degree of variability at all observable length scales) [*Mandelbrot*, 1983]. Thus, a more accurate description of "variable" slip is in the fractal sense, where slip has a consistent

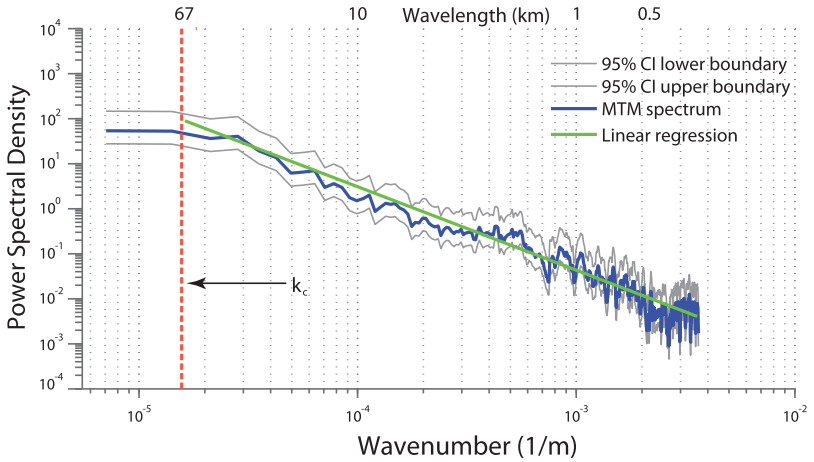

Figure 4. Power spectrum of the along-strike slip as a function of wave number (m^{-1}) in log-log space, computed using the multitaper method (MTM) [*Thomson*, 1982]. The 95% lower and upper confidence intervals are plotted as lower and upper gray lines, respectively. The β parameter is estimated using a Monte Carlo method with 10,000 simulations (green line showing the most probable fit) to the power spectral decay beyond the corner wave number (k_c) at the ~70 km wavelength. The Monte Carlo yields a β value of 1.87 ± 0.04 (95% confidence interval), with an R^2 of 0.80.

(power-law) decay of heterogeneity with decreasing length scale. That is, there is a power-law relation between the amplitude and wavelength of the slip distribution, where longer-wavelength slip perturbations have a larger amplitude and smaller wavelengths have smaller amplitudes (Figure 4). The linear relation between the Hurst exponent *H* (which characterizes the stochastic component of the data and gives a measure of the long-term memory) and the fractal dimension *D* in equation (3) (where *E* is the Euclidean dimension of the fractal medium), gives a Hurst exponent of 0.44 ± 0.04.

$$P(k) \propto k^{-\beta}, \tag{1}$$

$$D = \frac{5-\beta}{2}, \tag{2}$$

$$H = 1 + E - D. \tag{3}$$

A Hurst exponent less than 0.5 indicates that coseismic slip is not random, but rather is nonpersistent with a "short-memory" (i.e., neighboring points of displacement are correlated but tend to be further away from each other than random) [*Turcotte*, 1997]. In addition to applying the fractal analysis to the cumulative, projected slip profile (upper black line in Figure 3), we also applied it to the individual faults (colored lines in Figure 3) and found a similar result.

2.3. Measuring Off-Fault Deformation (OFD)

We measured OFD along the 1992 Landers surface rupture by comparing the COSI-Corr displacement data, which measures the total shear accommodated across a fault, to the displacement measured in the field, which represents the discrete component of displacement. Postearthquake field mapping of the surface rupture produced 763 displacement measurements [*Bryant*, 1992, 1994; *Liu et al.*, 2003, and references therein], where we only considered the horizontal component of displacement because our COSI-Corr measurements cannot constrain vertical deformation. Off-fault deformation (OFD) is calculated by simply taking the difference between our COSI-Corr displacement measurements (total displacement) and the field measurements (on-fault displacement), as described by equation (4).

$$\text{Off-fault deformation} = \text{COSI-Corr displacement} - \text{main strand field displacement}. \tag{4}$$

Field measurements are assumed to primarily capture the discrete, on-fault component of slip as they typically use piercing points taken over a 1–10 m wide, fault perpendicular aperture and therefore usually do not (and frequently cannot) include precise measurement of the complex, distributed off-fault deformation [*McGill and Rubin*, 1999; *Treiman et al.*, 2002; *Rockwell et al.*, 2002; *Shelef and Oskin*, 2010]. This assumption, however, forms a minor limitation of our calculation of OFD, as in some cases field geologists may

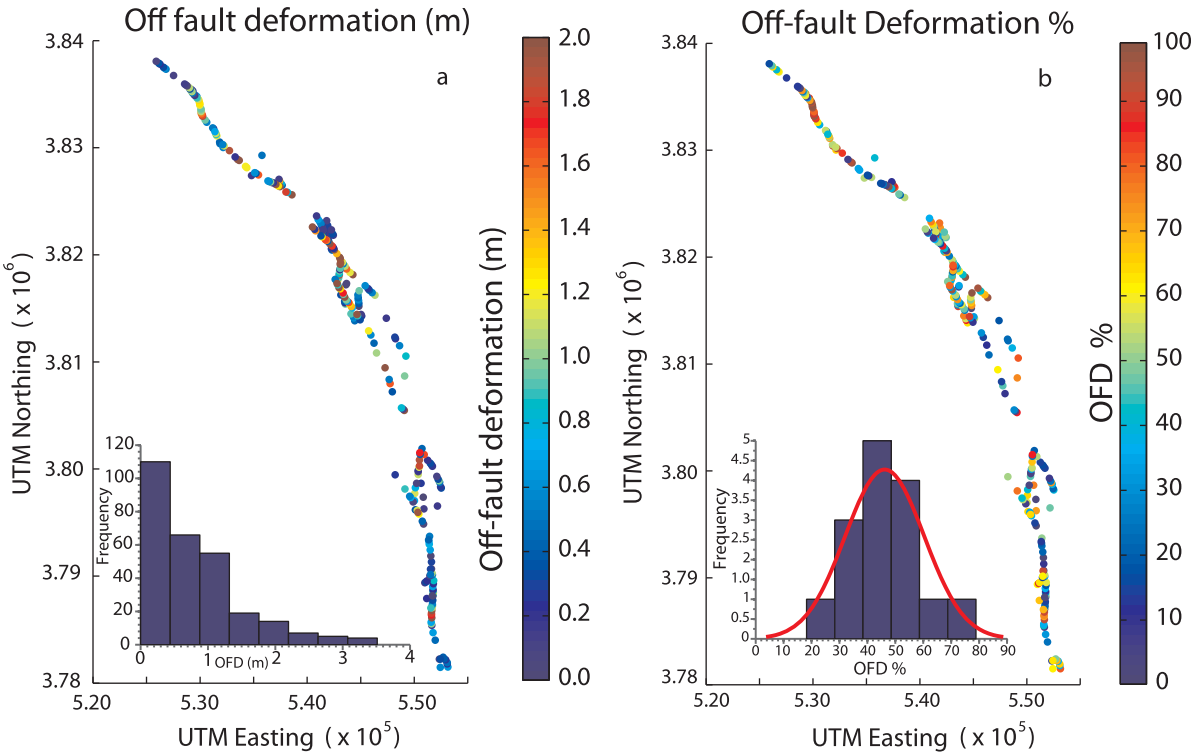

Figure 5. (a) Map view of the off-fault deformation (OFD) in meters. Points are computed from differencing the data in Figure 2a from Figure 2b. (b) Map view of OFD%. Qualitatively, the OFD% is smaller along structurally simple parts of the rupture (e.g., Johnson Valley fault) and largest in structurally complex areas (e.g., Homestead-Emerson stepover, bend in the Emerson fault and sites of branching of the rupture).

successfully capture some or all OFD (e.g., by using an offset feature that is sufficiently large to span the entire fault zone). However, such features, which are almost universally man-made, must be linear, orientated perpendicular to the fault, and have a precisely known preearthquake configuration. Unsurprisingly such features were rare along the Landers surface rupture and therefore this bias does not significantly affect our OFD data. Furthermore, postseismic deformation likely does not significantly bias our COSI-Corr comparison to the field measurements in calculating OFD, because, as mentioned above, a maximum of ~15 cm of postseismic afterslip was observed 7 years after the earthquake [*Fialko*, 2004] (a conservative value given our data are acquired 2 years after the earthquake) and also an amount barely detectable with our technique.

We determined the off-fault deformation at points along the surface rupture by iterating through every COSI-Corr displacement measurement in order to find the nearest corresponding field displacement point within a 138 m distance (stack width), and then computing the difference. This difference yields a single value for the OFD at that point along the rupture, following equation (4). In the 11 instances where field measurements are clearly collected as a transect across multiple, parallel fault strands, we sum all the field offsets. However, in instances where multiple field measurements are not strictly collected in such a manner and are heterogeneously distributed within a single COSI-Corr measurement zone (138 m along-strike distance), we treat these points as independent measurements and consider only the largest field displacement. Using only the largest field measurement therefore characterizes the discrete component of displacement occurring on the primary fault strand and thus the OFD calculation gives a consistent estimation of the amount of inelastic deformation occurring away from the main surface rupture. The output of this calculation gives a 2-D map of OFD at 280 points along the entire surface rupture (Figure 5). We find the OFD data follow an exponential distribution, where the median of 0.56 m is ~70% of the mean value of $0.81 + 0.12$ m (2σ measurement precision). Comparing each COSI-Corr displacement measurement with the corresponding field measurement indicates the former is systematically larger (Figure 6). The correlation between the COSI-Corr and field displacement data is determined using a total least squares method, which yields a slope of 1.47 that characterizes the relative difference in magnitude between the two data sets.

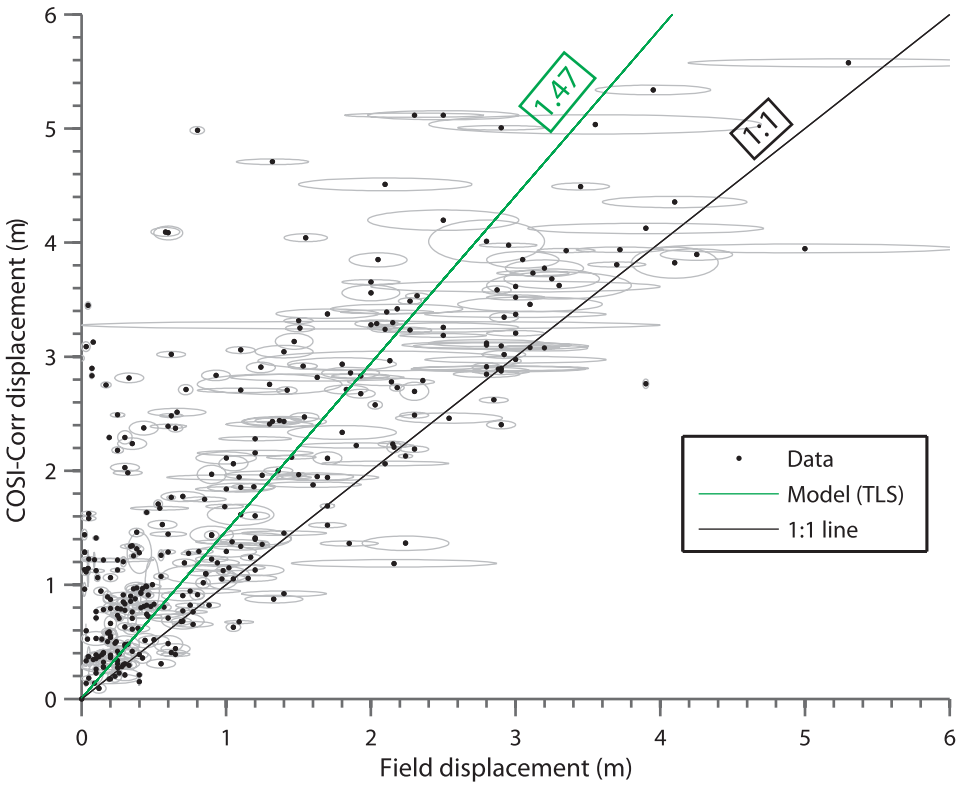

Figure 6. Correlation plot of field displacements versus our COSI-Corr displacement measurements. The gray ellipses denote the 1σ error in both the *x* and *y* direction. Using a total least squares approach to fit a linear regression to the observed data, which accounts for errors in the *x* and *y*, the best fitting model has gradient of 1.47, with R^2 of 0.77, which is in contrast to the black line with gradient of one.

As well as calculating OFD in meters we also express it as a percent of deformation that occurs off the main fault, herein known as OFD%. This is simply defined as [OFD (m)/COSI-Corr displacement (m)] $\times$ 100, where at each point along the rupture we normalize for the amount of total displacement. This normalization is performed for two reasons: (i) we want to know the relative amount of deformation that is accommodated off the fault in relation to how much is accommodated on the discrete, primary strand. (ii) The amount of OFD will arbitrarily be a function of the amount of displacement at a given site, where the displacement itself varies along the rupture. This allows for a direct comparison of its variability along the length of the surface rupture. The OFD% is markedly larger in areas of structural complexity, such as stepovers (e.g., the Kickapoo and Homestead-Emerson step overs), bends in the fault (notably at the bend of the Emerson fault as it merges into the Camp Rock fault), branching of the main-strand rupture (as seen in the central portion of the Johnson Valley fault) and the southern termination of the Landers rupture (Figure 5b). To calculate a reliable mean OFD% value for the entire Landers surface rupture, we spatially resampled the OFD data in order to correct for their spatial heterogeneity, which if unaccounted for would cause a bias. Downsampling the OFD data into 15 regions equally spaced along the rupture evenly reweights the data, thereby correcting for the issue of spatial heterogeneity. From this procedure, we find OFD% for the Landers earthquake has a mean value of 46 $\pm$ 10% (1σ), following a normal distribution as confirmed by a Lilliefors test.

2.4. Measuring Fault Zone Width (FZW)

The fault zone width (FZW) is defined as the fault-perpendicular extent of observable surface shear on either side of the primary, localized fault trace. From the correlation maps the FZW is measured as the extent of detectable pixel movement found adjacent to a primary main fault strand. Significantly, our method of measuring the FZW is insensitive to the physical mechanism(s) accommodating shear across the fault zone (e.g., warping, block rotation, grain sliding, or folding), because COSI-Corr is simply detecting shifting of features in the photos that exist on either side of the primary, discrete fault. Thus, our FZW measurements physically represent the width of a shear zone accommodating horizontal deformation of $>$10 cm (our detection limit) by any number of possible deformation mechanisms.

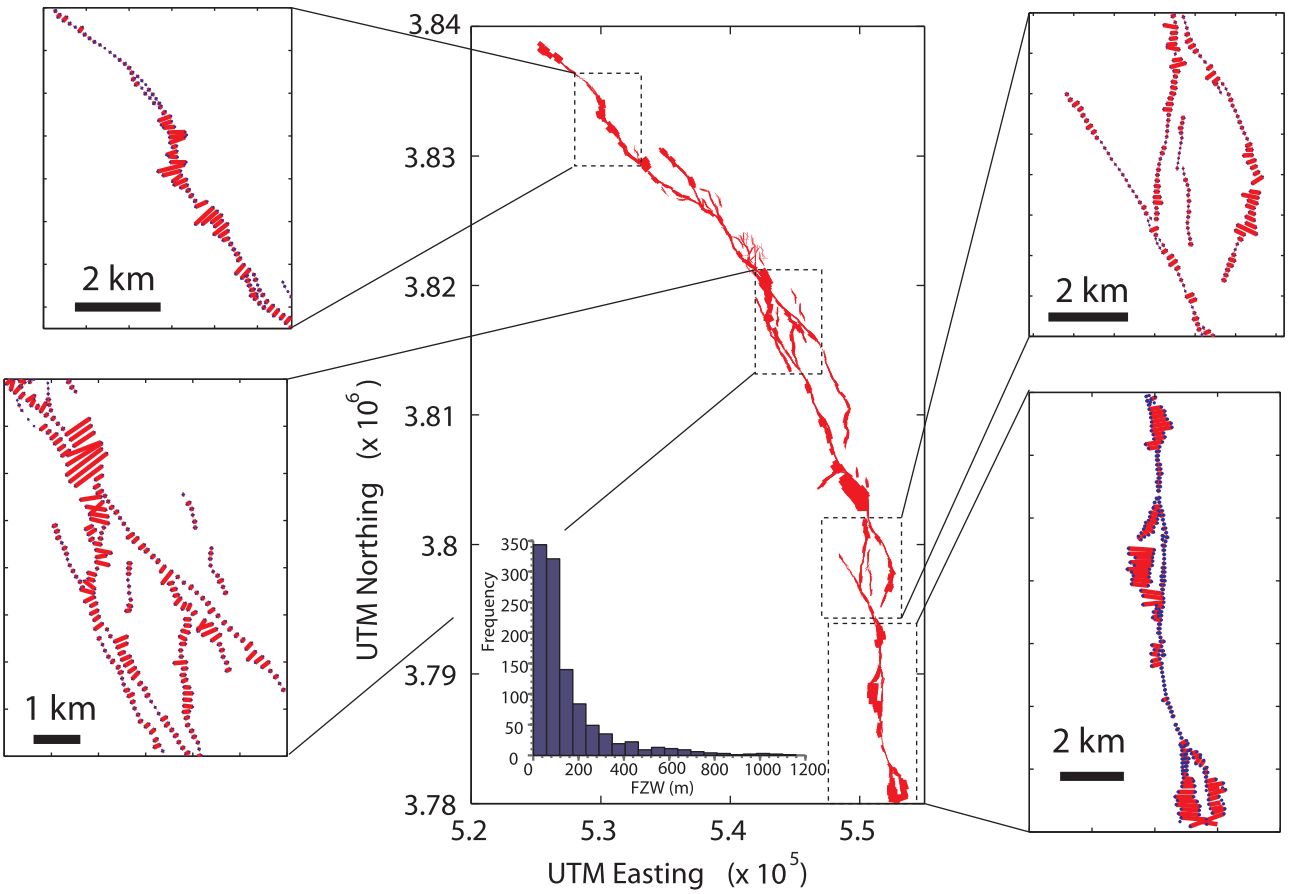

Figure 7. Map view of all 1060 fault zone width (FZW) measurements, spaced every 138 m along the surface rupture. The FZW is plotted as red bars with the histogram in lower left corner. Inset images shows examples where the FZW increases where the rupture becomes structurally complex (e.g., at branches, bends, or terminations).

A second set of synthetic tests were employed to investigate the degree of artificial smoothing of the tectonic signal, caused by the use of a sliding window, and how this affects the estimation of the FZW. This smoothing results from the assumption that during the correlation process the subset of pixels evaluated within the sliding window have constant displacement. To correct for this oversimplification, we created a series of synthetic faults of known widths (between 1 and 155 m wide), and after correlation of the sheared image with a different, un-disturbed image, we measured the smoothed, synthetic FZW. This gave an empirical calibration curve (Figure S2), which allows us to reliably recover the true FZW from the smoothed equivalent. Our results demonstrate that we can reliably resolve a FZW of $>$18 m (anything less is still measured, although the signal saturates and becomes too narrow to be fully resolved).

To measure the FZW of the Landers rupture we used the same stacked profiles that defined the fault displacement to make a total of 1060 measurements (Figure 7). From these measurements we found a mean FZW of 154 m, median of 96 m, and a maximum of 1160 $\pm$ 12 m (2σ), (located north of the Kickapoo stepover). The FZW varies smoothly along the Landers rupture and is most pronounced in regions of structural complexity, such as stepovers, kinks, and bends in the main fault trace, in a manner similar to the OFD result. Notably wide fault zones occur in the northern area of the Kickapoo stepover, in the northern region of the Homestead-Emerson stepover, at the southern termination of the rupture and at a 33° bend in the Emerson fault. The deformation width defined by the brittle, discrete faults, mapped by field geologists shortly after the earthquake [*Bryant*, 1992, 1994; *Liu et al*., 2003, and references therein], provides an independent constraint on the fault width, and agrees well with many of our FZW measurements. However, in some places along the rupture our FZW measurements (a shear zone accommodating deformation down to the 10 cm scale) are significantly wider than the fault zone defined by discrete faults mapped in the field (displacements generally mapped down to the 2 cm scale). This discrepancy suggests that discrete, brittle

faulting is not the only physical mechanism accommodating strain and that other processes, which are not easily observed in the field, exist, such as warping, folding, granular flow, block rotation, or microcracking, in agreement with *McGill and Rubin* [1999].

3. Discussion

3.1. Factors Controlling Off-Fault Deformation (OFD) and Fault Zone Width (FZW)

Both the off-fault deformation (OFD) and fault zone width (FZW) measurements exhibit large spatial variability, raising the issue of what observable parameters could be the cause. Our catalog of 280 OFD measurements and 1060 FZW measurements provides a large database with which we can test various hypotheses. Here we apply a statistical analysis in order to understand the range of possible parameters that likely controls the variability of strain localization.

First, we considered the role played by the macroscopic, first-order fault zone structural complexity (complexity that varies on the 10^4 m length scale) in controlling the OFD and FZW. We characterized the structural complexity of segments of the Landers fault system by constructing a qualitative, subjective classification scheme that varies from 1 to 5, with 5 being the most structurally complex and 1 the simplest. Our criteria for determining the relative level of fault structural complexity of a region includes the number of faults in the given area, the degree of segmentation and number of geometrical complexities such as bends, kinks, or steps (Figure 8c).

We find OFD positively correlates with the macroscopic structural complexity of the fault system, as intuitively expected, and as illustrated by the linear regression in Figure 8a. Specifically, where the fault is more complex, with diffuse faulting spread over an area, we observe systematically larger OFD%. In contrast, along structurally simple sections of the fault (e.g., single fault strands), considerably less strain was accommodated off the main surface rupture. In general, deformation accommodated off the main fault increases by $\sim$10% from one level of our relative structural complexity index to the next, as expressed by the gradient in our linear regression (Figure 8a).

The FZW is found to exhibit a positive, but weak, correlation with the fault zone complexity (Figure 8b). Specifically, a Monte Carlo simulation involving 10,000 iterations shows the most probable relation between the FZW and fault zone complexity is positive (gradient of 0.1). However, due to the large scatter in the data (as illustrated by the "error" bars in Figure 8b, which show the standard deviation of the data, as opposed to the standard error in the estimate of the mean), there is ambiguity on the range of possible gradients that could fit the data (1σ for slope of 0.1). Nevertheless, as noted above, a basic observation from our analysis is that the FZW widens in areas of increased structural complexity, such as stepovers or fault terminations, and narrows in areas of simple fault structure.

Field studies of other surface ruptures have documented that the FZW and OFD vary at least in some instances, according to the type of the near-surface materials [e.g., *Rockwell et al*., 2002; *Treiman et al*., 2002; *Van Dissen et al*., 2011; *Teran et al*., 2011; *Zinke et al*., 2014. To investigate this, we used geologic maps [*Dibblee*, 1964a, 1964b, 1967a, 1967b, 1967c] to help categorize the geologic units along the Landers rupture. We hypothesized that the more consolidated geologic units (e.g., bedrock) would yield lower magnitudes of OFD and narrower fault zones, and vice versa for less consolidated units (e.g., young alluvial sediments). We also assign a third classification for near-surface materials, termed "sediment-bedrock interface," which describes areas of the rupture where sediment juxtaposes against bedrock. We find distinct groupings of OFD associated with the type of near-surface materials through which the rupture propagated (Figures 9a–9c). As might be expected, "sediment-sediment" units show large amounts of OFD% (mean of $49 \pm 24\%$ [1σ]), while "basement-basement" units show a surprisingly, large and similar amount of distributed deformation (mean of $52 \pm 25\%$ [1σ]). The "sediment-basement interface" classification in Figure 9b shows a positively skewed distribution toward strain being more localized, and exhibits lower magnitudes of OFD% (mode of 19%) than other near-surface materials.

The FZW also exhibits a distinct and similar pattern as OFD, with the type of near-surface material (Figures 9d–9f). Specifically, where the rupture propagated along "basement-sediment interface," we find the narrowest FZW's (mean of 55 m), conversely at sites of "sediment-sediment" material the rupture exhibits wider zones of deformation (mean of 155 m) and in "basement-basement" material we find unusually wide FZWs

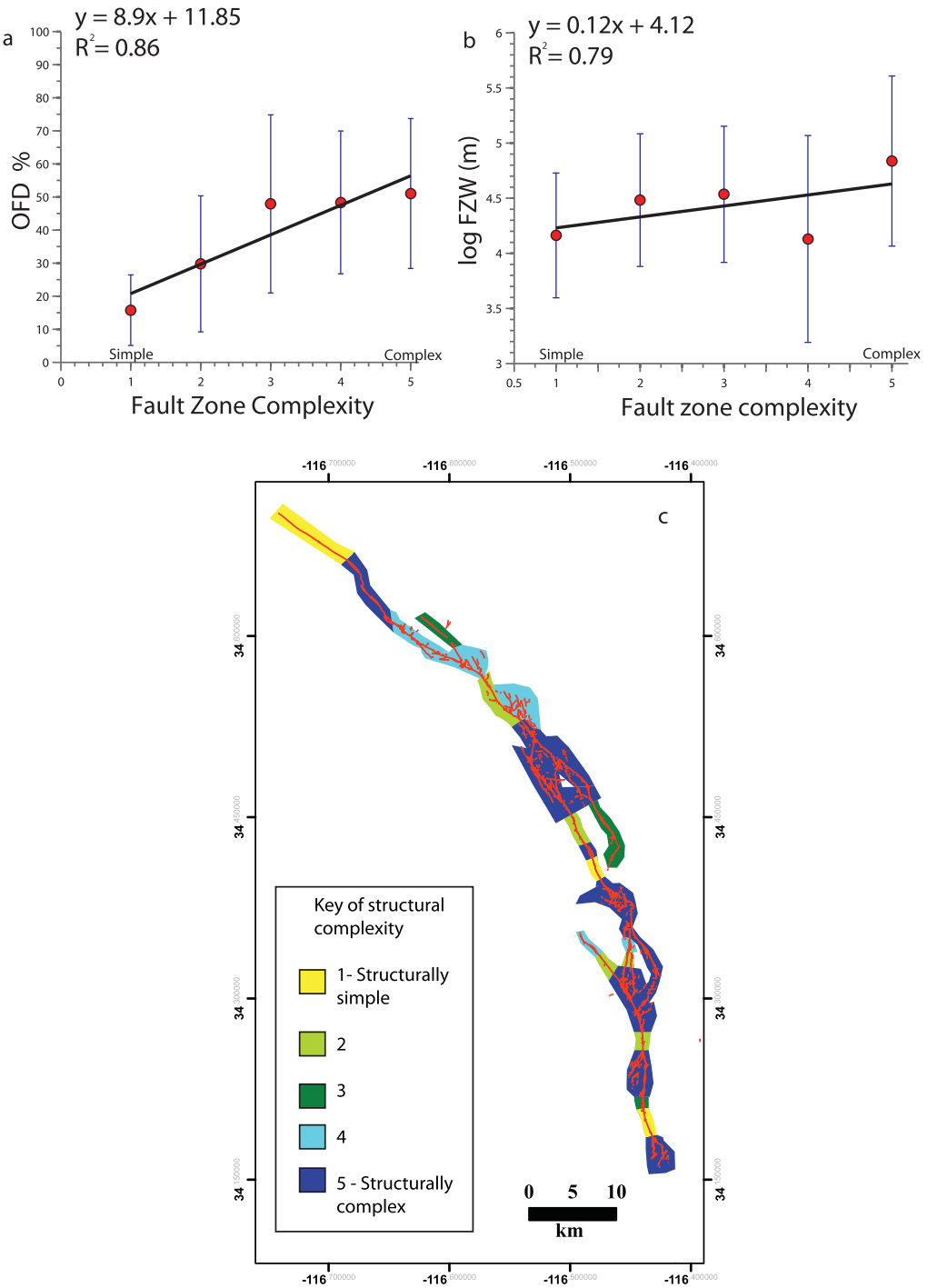

Figure 8. (a) Percent of off-fault deformation (OFD%) plotted as a function of the fault zone complexity. (b) FZW plotted as a function of fault zone complexity. A Monte Carlo simulation with 10,000 iterations yields an estimate of the slope for the linear regressions in Figure 8a as 8.9 ± 4.6 (1σ) and for Figure 8b as 0.1 ± 0.1 (1σ), where the slope in Figure 8b exhibits large ambiguity due to the large variability of the data. We find a p value of 0.34 indicating weak statistical significance. (c) Map view of Landers surface rupture shown in red lines [*Liu et al.*, 2003]. Structural complexity of the fault zone is delineated by the colored polygon areas, classified from 1 to 5, with 1 being the structurally simplest and 5 the most complex. We classify the structural complexity on the 1–10 km length scale so to analyze the macroscopic complexity of the mapped fault traces, with the following criteria defining each index: (1) straight, continuous single-stranded. (2) Segmented, semicontinuous trace with smaller secondary faulting. (3) Dual-stranded or greater number of secondary faulting. (4) Abundant secondary faulting, subtle-moderate bends in fault trace. (5) Step overs, highly diffuse areas of faulting, macroscopic fault bends. We note that the width of the deformation was not used as a criterion of fault zone complexity and these parameters are treated independently.

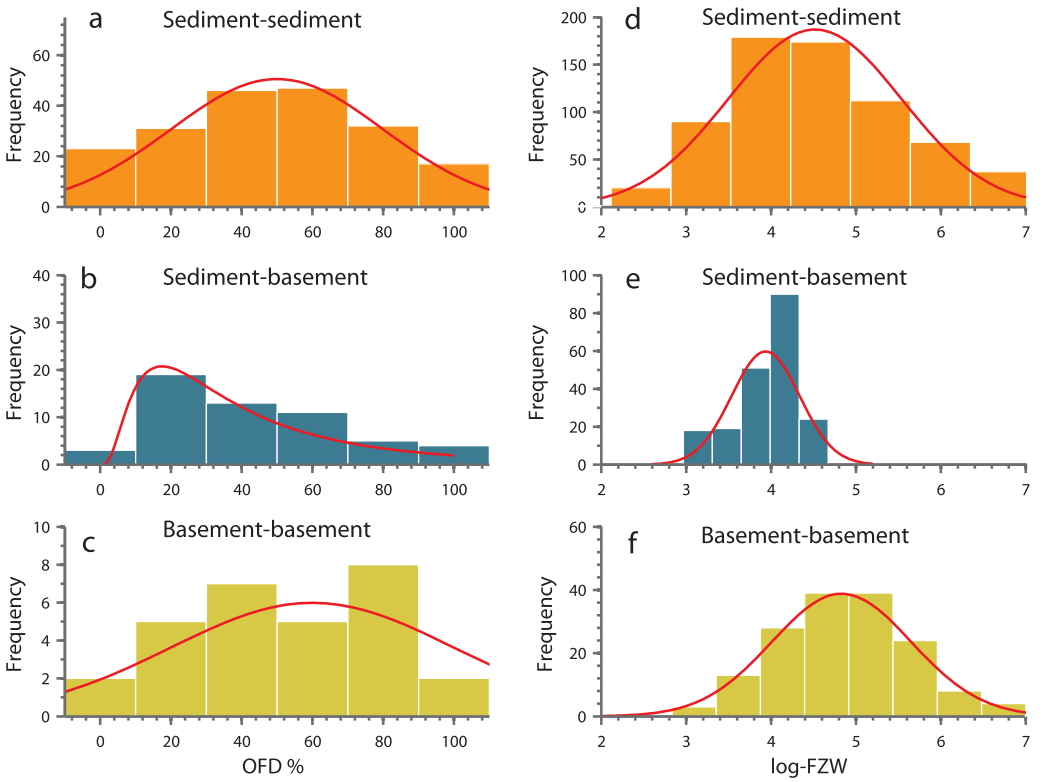

Figure 9. (a, b, c) Histograms of OFD% subdivided into "sediment-sediment" (mean 48%), "sediment-basement interface" (mode of 19%, which is the global maximum of the population), and "basement-basement" lithologies (mean 52%), respectively. Red lines show the best fitting distributions which are normal, as confirmed by a Lilliefors test, except for Figure 9b which is a positively skewed distribution. (d, e, f) FZWs plotted with same lithological classification, which are lognormal as confirmed by Lilliefors tests, except for Figure 9e which is only slightly negatively skewed. "Sediment-basement interface" shows the narrowest FZW with mean of 55 m and median of 58 m, "sediment-sediment" shows wide FZW with mean of 155 m and median of 84 m and "basement-basement" shows unusually wide FZWs with mean of 173 m and median of 129 m.

(mean of 173 m). Interestingly, the smallest magnitudes and narrowest zones of inelasticity are observed in areas of "basement-sediment interface" (Figures 9b and 9e), which likely results from efficient localization at these sites along strong mechanical contrasts [*Martel et al*., 1988; *Bruhn et al*., 1994; *Sibson*, 2003; *Ben-Zion and Sammis*, 2003]. We also found that where the rupture propagated through "basement-basement" material, the FZWs are unusually wide and OFD surprisingly large, compared to other material types. We attribute these somewhat counterintuitive results because the vast majority of bedrock outcrop (84%) occurs within the structurally complex Homestead-Emerson stepover.

We compared several parameters with the surface deformation pattern, specifically the fault complexity, the type of near-surface materials, lateral distance to bedrock (proxy for sediment thickness), fault orientations (proxy for relation of fault to regional stress field), and inferred age of alluvial fans (proxy for degree of lithification). Aside from the structural complexity of the surface rupture and type of near-surface materials through which the rupture propagated, we note for most of the tested parameters there was no clear correlation with OFD and FZW (see Figures S5–S17). We suspect that the overarching correlation we observe between OFD and the structural complexity of the faults likely obscures and complicates isolating the effects of other parameters.

Furthermore, an added complication in our analysis is that a component of the variability in the OFD data is likely statistical noise, derived from inaccuracies of the reported field displacement measurements. Such inaccuracies can arise due to the subjective and difficult nature of measuring the true displacement from geomorphic piercing points where the exact prerupture geometry is not known [*McGill and Rubin*, 1999; *Arrowsmith and Rockwell*, 2012; *Salisbury et al*., 2012; *Gold et al*., 2013; *Madden et al*., 2013; *Scharer et al*., 2014]. Over or underestimation of the true fault displacement by field surveys will cause under or overestimation of OFD in our calculation [equation (4)], respectively. For this reason, in our analysis we group larger

subsets of OFD data (e.g., Figures 8 and 9) which allows suppression of this effect and to more reliably constrain possible correlations.

Our analysis of the Landers rupture reveals a mean value of 46 ± 10% (1σ) of the surface deformation was accommodated off-the primary fault (although it should be noted OFD exhibits significant spatial variability along the rupture from 0 to 90%). But is this large average value physically reasonable? Following the quasi static model of fault evolution, faults that have experienced small cumulative displacements, such as those involved in the Landers rupture (~3.5 km) [*Jachens et al*., 2002], have not accommodated sufficient strain to localize into simple, organized, efficient systems [e.g., *Wesnousky*, 1988, 1990; *Frost et al*., 2009], and therefore we expect a relatively large value of OFD [*Dolan and Haravitch*, 2014]. Moreover, our value of OFD agrees well with the results of *Shelef and Oskin* [2010], who found OFD of up to 46 ± 6% along the comparably structurally immature (3.5 km cumulative slip) [*Bartley et al*., 1992] Harper Lake fault.

Damage zones of reduced rigidity with a width of ~2 km have been observed surrounding the Landers surface rupture using InSAR data [*Fialko et al*., 2002], and also for the San Andreas, Calico and San Jacinto faults using geodetic and seismic data [*Eberhardt-Phillips and Michael*, 1993; *Allam and Ben-Zion*, 2012; *Cochran et al*., 2009; *Lindsey et al*., 2013]. In contrast, the zone of inelastic deformation that we document from the Landers earthquake is much narrower, with a mean FZW of 154 m. This is similar to the results of seismic studies using fault zone trapped waves and waves of reduced velocity, which reveal a damage zone width of ~100 m for the Landers fault system [*Li et al*., 1998; *Peng et al*., 2003]. This discrepancy between our single-event data and observations of damage zones reflecting cumulative deformation may be a manifestation of progressive localization of near-surface damage and structural simplification of the faults that ruptured in the Landers earthquake over geologic time. However, we reiterate that our analysis can only observe surface deformation to a minimum threshold of ~10 cm using the COSI-Corr technique. Thus, it is likely that minor amounts of distributed deformation could be accommodated in a deformation zone wider than what is resolvable in our analysis. Nonetheless, our data demonstrate that inelastic deformation was predominantly localized to within a <200 m wide zone along the faults, much narrower than the typical ~2 km wide deformation zones that likely reflect the entire, cumulative history of deformation.

There is likely a complex combination of multiple parameters that control strain localization, many of which remain poorly constrained or are not accounted for at all in this analysis. For example, the local static and dynamic stresses, the dynamic rupture velocity, and fracture energy are thought to strongly control the deformation pattern around the propagating rupture tip [e.g., *Ben-Zion and Andrews*, 1998; *Ben-Zion and Shi*, 2005; *Sammis et al*., 2009; *Avouac et al*., 2014]. Knowledge of the characteristics of the rupture processes at the spatial scales (>100 m) used here and a more robust characterization of the measurement uncertainty in field offset measurements, would serve to improve analyses of strain localization. Additional measurements of surface deformation from other large-magnitude, structurally simpler ruptures will also help to further clarify the characteristics of coseismic strain localization.

3.2. Coseismic Slip Variability

Understanding coseismic, surface slip behavior can provide useful information on fault zone mechanics, the potential for faults to link together to generate large earthquakes, the dynamic rupture process, and the likely endpoints of ruptures [e.g., *Wesnousky*, 2006, 2008; *Elliott et al*., 2009; *Oskin et al*., 2012; *Rockwell and Klinger*, 2013]. Our spatially consistent data set documenting fault displacement as well as OFD allows for a detailed discussion of the faulting kinematics, coseismic slip variability, and dynamic rupture behavior of the Landers earthquake.

Theoretical, analog, and geologic studies all suggest that rupture fronts dissipate fracture energy, and decelerate as they encounter zones of complex, diffuse deformation which in some cases leads to rupture cessation [e.g., *Segall and Pollard*, 1980; *Schwartz and Coppersmith*, 1984; *Barka and Kadinsky-Cade*, 1988; *Harris et al*., 1991; *Harris and Day*, 1993; *Duan and Oglesby*, 2005; *Wesnousky*, 2006; *Oglesby*, 2008; *Biegel et al*., 2008; *Elliott et al*., 2009; *Sammis et al*., 2009]. The location of two areas of reduced slip (termed "slip gaps" by *Spotila and Sieh* [1995]) along the surface rupture (labeled iii and iv in Figure 3), can be explained by their spatial relation to the structurally complex Kickapoo and Homestead-Emerson stepovers that in both cases lie directly to their south. At both structurally complex stepovers we found increased FZWs and OFD% (in agreement with *Michel and Avouac* [2006]), where the rupture also significantly decelerated, as revealed by seismic inversion studies [*Wald and Heaton*, 1994]. This relationship between abrupt changes in fault slip

and the presence of structural barriers that affect the rupture process has also been well documented in other earthquakes [e.g., *Aki*, 1979; *Spotila and Sieh*, 1995; *Klinger et al*., 2006; *Elliott et al*., 2009]. The OFD% and FZW also increases markedly toward the southern termination of the Landers rupture, which suggests that the more diffuse fault structure there likely acted as a barrier that arrested rupture propagation. In contrast, our measurements do not provide an explanation for the northern rupture termination where we observe low OFD and narrow FZWs, where slip was concentrated only within the uppermost few km along the Camp Rock [*Wald and Heaton*, 1994].

The coseismic slip profile for the Landers rupture exhibits strongly heterogeneous along-strike slip variability (Figure 3). There is no consensus as to whether along-strike coseismic slip variability observed at short spatial dimensions is a true reflection of the rupture process or is an artifact of inadequate characterization of fault displacements and/or missing OFD. For example, measurements of the coseismic slip from terrestrial lidar scanning along the M_w 7.2 El-Mayor earthquake suggest a smooth slip distribution at along-strike wavelengths $<$100 m, and that the slip variability observed in geological field measurements arise primarily from measurement noise [*Gold et al*., 2013]. In contrast, studies of coseismic slip distributions from the 1940 M_w 7.1 Imperial, 1999 M_w 7.5 Izmit, and 2001 M_w 7.9 Kokoxili earthquakes, using various field and remote-sensing techniques that incorporate OFD, suggest that slip variability is a real reflection of the rupture process [*Rockwell et al*., 2002; *Klinger et al*., 2006; *Rockwell and Klinger*, 2013]. Resolving whether coseismic slip is smooth or truly irregular at short length scales has important implications for understanding the physics governing the rupture process, and the estimation of paleoearthquake magnitudes from fault offsets.

As the along-strike slip variability exceeds that of the measurement error, this suggests the variability is a real signal, reflecting aleatory variability of the rupture process and is not derived from epistemic uncertainty (i.e., measurement noise). Our synthetic tests, which form an extensive error analysis of the measurement precision (see Figures S1–S4), have allowed us to quantify and incorporate the various sources of error that were previously thought to be the major source of the observed slip variability. Furthermore, the slip variability we observe includes OFD measured on average up to 154 m from the surface rupture (Figure 7), therefore indicating the variability we measure does not simply arise from missing distributed strain along-strike, as has been commonly assumed.

These observations raise an obvious question: Are there other potential explanations for the slip variability we observe? For example, highly diffuse, distal OFD that exists below our threshold of detection, if accounted for, could smooth the overall along-strike deformation profile. However, for this effect to discount the near-field variable slip would require low-amplitude deformation that occurs over wide fault-perpendicular regions (in order to be undetectable) that would also have to anti-correlate over the same short along-strike distances as the coseismic slip distribution, which seems physically unlikely. Nevertheless, the possible presence (or absence) of distal, diffuse OFD ($>$200 m from rupture) does not negate our observation that the deformation in the near-field (0–100's m from surface rupture) is variable. A second possible mechanism is that displacement variability could be explained by accommodation of slip in the fault-perpendicular direction. However, our measurements of fault-perpendicular displacement from the correlation results (Figure 1), indicate that such a mechanism cannot explain the lateral, along-strike slip heterogeneity because these displacements exist below the noise level (i.e., have an amplitude less than 10 cm).

Fractals are observed widely in many facets of earthquake behavior, such as the Guttenburg-Richter frequency-magnitude scale [*Gutenberg and Richter*, 1956; *Kanamori and Anderson*, 1975], seismicity distribution across faults [*Powers and Jordan*, 2010], fault surface roughness [*Brown and Scholz*, 1985; *Power et al*., 1988; *Biegel and Sammis*, 1989; *Power and Tullis* 1995; *Power et al*., 1988; *Lee and Bruhn*, 1996; *Renard et al*., 2006; *Candela et al*., 2009], spatial structure of faults [*Aviles et al*., 1987; *Okubo and Aki*, 1987], and spatial distributions of earthquake hypocenters [*Robertson et al*., 1995]. Noting that the slip distribution is highly heterogeneous, we used a spectral analysis to show that the slip distribution is self-affine fractal (Figure 4), with a dimension (D) of 1.56 $\pm$ 0.04. We believe this is the first study to conclusively find, with direct observations, that coseismic slip is scale-invariant (within the observed wavelengths) and self-affine fractal. Essentially fractal slip means a power law describes the relation between the slip amplitude and wavelength over a broad spectrum, indicating that the seemingly complex "variability" actually has a simple and predictable underlying structure. This is in agreement with modeled fault slip distributions determined from inversion of seismic and geodetic data, which also exhibit a fractal structure [*Mai and Beroza*, 2002]. *Dunham et al.* [2011] generated 2-D numerical

simulations of dynamic rupture propagation along a non-planar fault of fractal roughness surrounded by a damage zone, and found that geometrically rough faults produce significant along-strike slip variability. They suggested that stress variations along the fault result from surface roughness, which in turn accelerates and decelerates the rupture front, causing slip heterogeneity Similarly, *Dieterich and Smith* [2009], using a quasi-static, numerical model, also found a nonplanar, fractal fault surface produces variable along-strike slip. They attributed highly variable slip to the generation of backstresses from the geometric irregularities of the fault surface that acted to resist the applied Coulomb stress driving slip. Thus, if the slip variability observed here is a manifestation of fault roughness, it is not surprising to find that slip is fractal, given that many natural fault surfaces also display self-affine fractal roughness [e.g., *Power and Tullis*, 1995; *Lee and Bruhn*, 1996; *Renard et al*., 2006; *Candela et al*., 2009]. The Hurst exponent of 0.44 ± 0.04 we derived from our analysis of the Landers slip distribution and equation (3) indicates that coseismic slip was nonpersistent. This value is similar to that found by *Powers and Jordan* [2010] from seismicity distributions across aftershock-dominated, small faults in southern California (such as the Landers-type faults), where the authors also attributed the observed power-law decay of seismicity distributions to fault surfaces of fractal roughness. The observed antipersistence of the slip distribution is the expected result if slip is controlled by roughness of the fault plane. Each asperity on a fault plane can be viewed as a restraining bend followed by a releasing bend (or vice versa). Fault roughness can be viewed as a fractal distribution of such asperities. In this view, low slip at a restraining bend is necessarily followed by high slip in the associated releasing bend, resulting in an antipersistent slip distribution—as observed.

Our measured slip profile exhibits an apparent roll-off of the spectra at $\sim$70 km (k_c in Figure 4), which is arbitrarily related to the length of the Landers rupture. This indicates fractal slip has an upper physical limit and suggests fractal behavior is limited to a certain range of spatial frequency bands. We hypothesize that if slip variability is primarily a result of the fault geometrical roughness, then the lower physical limit could be set by smoothing of the fault surfaces due to abrasional wear and fracturing, which would alter the fractal properties of the fault surface (initially) at smaller wavelengths. Specifically, this simple mechanism would cause prefential destruction of smaller, more fragile asperities, while larger-wavelength asperities, which are physically more robust, will survive, as documented by *Sagy et al*. [2007], and in the slip spectra (Figure 4) would produce a second roll-off or "whitening" at higher wave numbers. However, as our Nyquist frequency is 69 m (smallest reliably resolvable length scale, defined as half the sampling frequency of 138 m), our data cannot directly resolve the expected lower limit to "band-limited" fractal slip. Our results, however, are not necessarily incompatible with those of *Gold et al*. [2013], who found using T-lidar data that slip over $<$100 m along-strike length scales along the El-Mayor 2010 earthquake, is smooth. Fractals imply scale-invariant behavior, and we postulate that smaller-amplitude slip variability could be further embedded within an apparently smooth slip profile that would be too subtle to detect given the precision of restoring geomorphic features using the T-lidar data ($2\sigma \pm 0.12$ m). This would suggest that the smooth profile is a good approximation of the first-order slip variability occurring over the $\sim$100 m length scale, but that smooth slip is not a true reflection of the underlying rupture process. In order to resolve this issue, would require ultra-high detailed measurements of fault slip that can detect centimeter-scale slip variability over $<$100 m along-strike length scales.

3.3. Implications for Slip Rates and Seismic Hazard

The presence of significant inelastic strain accommodated over a finite fault width along the Landers rupture has important implications for the use of any surface fault offset measurements, especially for estimates and interpretation of geologic fault slip rates and paleo-earthquake magnitudes. For example, if slip rate studies are conducted within a narrow aperture (i.e., over a few meters to tens of meters), restoration of geologic piercing points will likely miss a component of off-fault deformation, thus causing an underestimation of the fault slip rate. Such possible underestimation of fault slip rates, which are used as basic input for probabilistic seismic hazard assessment (PSHA) models, would lead to an underestimation of the potential seismic hazard of a region.

Variation of slip over short along-strike distances observed from the Landers data has direct implications for estimating the magnitude of paleo-earthquakes using geologic fault offsets. Specifically, the occurrence of along-strike coseismic slip variability introduces large ambiguity and error into what possible earthquake magnitude could have produced the observed geologic fault offset [*Rockwell et al*., 2002; *Biasi and Weldon*, 2006]. Furthermore, variable slip also implies that studies attempting to reconstruct slip profiles of historic

earthquakes from a stretch of fault, must be careful when trying to correlate offsets along-strike [e.g., *Zielke et al*., 2012].

A simple strategy to avoid underestimating slip rates due to the presence of sometimes unobservable inelastic, off-fault deformation is to project piercing points over a distance that traverses the entire fault zone. But this begs the question, what is the necessary length scale to capture all the deformation accommodated by an immature fault? The mean width of deformation of the Landers rupture derived from 1060 FZW measurements is ~150 m (or ~75 m from either side of the fault trace). We suggest that this is a conservative distance to adequately capture the majority of deformation across a fault zone with similar structural maturity to the faults involved in the Landers event. These FZW measurements thus provide useful information for future geotechnical zoning studies, as it will provide constraints on the width of the fault-surface-rupture hazard zone, where we would expect permanent ground deformation and direct destruction to engineered structures [*Chen and Petersen*, 2011; *Petersen et al*., 2011] These results which show significant off-fault surface deformation accommodated within these fault zones, reinforce the wisdom of fault "set-backs" such as those mandated by California Alquist-Priolo zones.

4. Conclusions

We developed a methodology to constrain the near-field, surface deformation pattern, that facilitates measurement of the coseismic slip distribution, off-fault deformation, and fault zone width using cross correlation of pre and postevent aerial photographs. This methodology is highly versatile and can be applied to historic and recent earthquakes in a cost-effective manner. This approach is also a useful complement to field investigations, as well as other remote sensing techniques, such as SAR interferometry, where there is typically a lack of data within 1–2 km of the rupture.

We applied our methodology to successfully constrain the near-field surface deformation pattern of the 1992 M_w 7.3 Landers earthquake and the full coseismic slip distribution down to 10 cm precision. Analysis of this data set shows that the Landers earthquake accommodated 46% of total surface strain as off-fault deformation over a mean deformation-zone width of 154 m. We also find that the Landers coseismic slip distribution exhibits a consistent degree of variability at all observable length scales, and that the variation is neither an artifact, nor random, but rather is fractal. We attribute the fractal behavior of coseismic slip to a fault surface of fractal roughness that likely alters the local stress.

Our analysis indicates that the structural complexity of the fault zone is the dominant control on the magnitude and width of surface deformation. Off-fault deformation and fault zone widths are largest in stepovers, kinks, and bends in the faults, as well at the southern termination of the Landers rupture. We also observe a correlation with the type of near-surface material through which the rupture propagated, with surface rupture along bedrock-sediment interfaces generating less off-fault deformation with relatively narrower fault zones, in contrast to wider, more distributed deformation where the rupture extended through sediments.

Acknowledgments

This research was funded by the US National Science Foundation (NSF EAR-1147436 grant to Dolan). We thank Amir Allabush for helpful discussions and reviews of an early draft of the paper and Jerry Treiman for his help in acquiring additional field measurements of the Landers earthquake. Finally we thank Mike Oskin, Ramon Arrowsmith and one anonymous reviewer for their help improving an earlier version of the manuscript. We thank the USGS for the EarthExplorer website (http://earthexplorer.usgs.gov/), which greatly simplified access to the aerial photographs used in this study. SPOT5 images were acquired from the coauthors S.L. and J.H.

References

Aki, K. (1979), Characterization of barriers on an earthquake fault, *J. Geophys. Res.*, *84*, 6140–6148.

Allam A. A., and Y. Ben-Zion (2012), Seismic velocity structures in the Southern California plate-boundary environment from double-difference tomography, *Geophys. J. Int.*, *190*, 1181–1196.

Arrowsmith, J. R., and T. K. Rockwell (2012), Repeatability, accuracy, and precision of surface slip measurements from high-resolution topographic data: Collaborative research with Arizona State University and San Diego State University, final technical report, U.S. Geol. Surv. Natl. Earthquake Hazard. Reduct. External Res. Program, USGS Award Number G11AP20029 (ASU) & G11AP20020 (SDSU), Reston, Va. [Available at https://www.google.com/url?sa=t&rct=j&q=&esrc=s&source=web&cd=1&cad=rja&uact=8&ved=0CB4QFjAA&url=http%3A%2F%2Fearthquake.usgs.gov%2Fresearch%2Fexternal%2Freports%2FG11AP20029.pdf&ei=jYw2VYzqO8vyoASut4HQDQ&usg=AFQjCNHzUiycQqCQ2L7Vmw5jMzGwd7u6Cw&bvm=bv.91071109,d.cGU.]

Aviles, C. A., C. H. Scholz, and J. Boatwright (1987), Fractal analysis applied to characteristic segments of the San Andreas Fault, *J. Geophys. Res.*, *92*, 331–344.

Avouac, J. P., F. Ayoub, S. Leprince, O. Konca, and D. Helmberger (2006), The 2005, Mw 7.6 Kashmir earthquake, rupture kinematics from sub-pixel correlation of ASTER images and seismic waveforms analysis, *Earth Planet. Sci. Lett.*, *249*(3–4), 514–528.

Avouac, J. P., F. Ayoub, S. J. Wei, J. P. Ampuero, L. S. Meng, S. Leprince, R. Jolivet, Z. Duputel, and D. Helmberger (2014), The 2013, Mw 7.7 Balochistan earthquake, energetic strike slip reactivation of a thrust fault, *Earth Planet. Sci. Lett.*, *391*, 128–134, doi:10.1016/j.epsl.2014.01.036.

Ayoub, F., S. Leprince, and J. P. Avouac (2009), Co-registration and correlation of aerial photographs for ground deformation measurements, *ISPRS J. Photogramm. Remote Sens.*, *64*(6), 551–560.

Barka, A. A., and K. Kadinsky-Cade (1988), Strike-slip fault geometry in Turkey and its influence on earthquake activity, *Tectonics*, *7*, 663–684.

Bartley, J. M., A. F. Glazner, J. M. Fletcher, M. E. Martin, and J. D. Walker (1992), Amount and nature of dextral off-set on Neogene faults near Barstow, California, *Eos Trans. AGU*, *73*, 363.

Ben-Zion, Y., and D. J. Andrews (1998), Properties and implications of dynamic rupture along a material interface, *Bull. Seismol. Soc. Am.*, *88*, 1085–1094.

Ben-Zion, Y., and C. G. Sammis (2003), Characterization of fault zones, *Pure Appl. Geophys.*, *160*, 677–715.

Ben-Zion, Y., and Z. Shi (2005), Dynamic rupture on a material interface with spontaneous generation of plastic strain in the bulk, *Earth Planet. Sci. Lett.*, *236*, 486–496, doi:10.1016/j.epsl.2005.03.025.

Ben-Zion, Y., Z. Peng, D. Okaya, L. Seeber, J. G. Armbruster, N. Ozer, A. J. Michael, S. Baris, and M. Aktar (2003), A shallow fault-zone structure illuminated by trapped waves in the Karadere-Duzce branch of the North Anatolian Fault, western Turkey, *Geophys. J. Int.*, *152*, 699–717, doi:10.1046/j.1365-246X.2003.01870.

Biasi, G. P., and R. J. Weldon (2006), Estimating surface rupture length and magnitude of paleoearthquakes from point measurements of rupture displacement, *Bull. Seismol. Soc. Am.*, *96*, 1612–1623, doi:10.1785/0120040172.

Biegel, R. L., and C. G. Sammis (1989), The frictional properties of a simulated gouge having a fractal particle distribution, *J. Struct. Geol.*, *11*(7), 827–846, doi:10.1016/0191–8141(89)90101-6.

Biegel, R. L., C. G. Sammis, and A. J. Rosakis (2008), An experimental study of the effect of off-fault damage on the velocity of a slip pulse, *J. Geophys. Res.*, *113*, B04302, doi:10.1029/2007JB005234.

Bridges, N. T., F. Ayoub, J.-P. Avouac, S. Leprince, A. Lucas, and S. Mattson (2012), Earth-like sand fluxes on Mars, *Nature*, *485*, 339–342, doi:10.1038/nature11022.

Brown, S. R., and C. H. Scholz (1985), Broad bandwidth study of the topography of natural rock surfaces, *J. Geophys. Res.*, *90*, 2575–2582.

Bruhn, R. L., W. T. Parry, W. A. Yonkee, and T. Thompson (1994), Fracturing and hydrothermal alteration in normal fault zones, *Pure Appl. Geophys.*, *142*, 609–644.

Bryant, W. A. (1992), Surface fault rupture along the Johnson Valley, Homestead Valley, and related faults associated with the M_s 7.5 28 June 1992 Landers earthquake, *Fault Eval. Rep. FER-234*, 21 p., scale 1:24,000, Calif. Dep. of Conserv., Div. of Mines and Geol., Sacramento, Calif.

Bryant, W. A. (1994), Surface fault rupture along the Homestead Valley, Emerson, and related faults associated with the M_w 7.3 28 June 1992 Landers earthquake, *Fault Eval. Rep. FER-239*, 18 p., scale 1:24,000, Calif. Dep. of Conserv., Div. of Mines and Geol., Sacramento, Calif.

Burgmann, R., P. A. Rosen, and E. J. Fielding (2000), Synthetic aperture radar interferometry to measure Earth's surface topography and its deformation, *Annu. Rev. Earth Planet. Sci.*, *28*, 169–209.

Cakir, Z., J. B. de Chabalier, R. Armijo, B. Meyer, A. Barka, and G. Pelzer (2003), Coseismic and early postseismic slip from the 1999 Izmit earthquake (Turkey), from SAR interferometry and tectonic field observations, *Geophys. J. Int.*, *155*, 93–110.

Candela, T., F. Renard, M. Bouchon, D. Marsan, J. Schmittbuhl, and C. Voisin (2009), Characterization of fault roughness at various scales: implications of three-dimensional high resolution topography measurements, *Pure. appl. Geophys.*, *166*, 1817–1851, doi:10.1007/s00024-009-0521-2.

Chen, R., and M. D. Petersen (2011), Probabilistic fault displacement hazards for the southern San Andreas Fault using scenarios and empirical slips, *Earthquake Spectra*, *27*(2), 293–313, doi:10.1193/1.3574226.

Chester, F. M., and J. S. Chester (1998), Ultracataclasite structure and friction processes of the Punchbowl fault, San Andreas system, California, *Tectonophysics*, *295*, 199–221.

Chester, J. S., F. M. Chester, and A. K. Kronenberg (2005), Fracture surface energy of the Punchbowl fault, San Andreas system, *Nature*, *437*, 133–136.

Cochran, E., Y. G. Li, P. M. Shearer, S. Barbot, Y. Fialko and J. Vidale (2009), Seismic and geodetic evidence for extensive, long-lived fault damage zones, *Geology*, *37*(4), 315–318, doi:10.1130/G25306A.1.

Dibblee, T. W. (1964a), Geological map of the Apple Valley & Ord Mountains quadrangle, San Bernardino 851 County, California, *U.S. Geol. Surv. Misc. Geol. Invest. Map, I-430*.

Dibblee, T. W. (1964b), Geological map of the Rodman Mountains quadrangle, San Bernardino 851 County, California, *U.S. Geol. Surv. Misc. Geol. Invest. Map, I-430*.

Dibblee, T. W. (1967a), Geological map of the Deadman Lake quadrangle, San Bernardino County, California, *U.S. Geol. Surv. Misc. Geol. Invest. Map, I-430*.

Dibblee, T. W. (1967b), Geological map of the Joshua Tree quadrangle, San Bernardino 851 County, California, *U.S. Geol. Surv. Misc. Geol. Invest. Map, I-430*.

Dibblee, T. W. (1967c), Geological map of the Old Woman Springs quadrangle, San Bernardino 851 County, California, *U.S. Geol. Surv. Misc. Geol. Invest. Map, I-430*.

Dieterich, J. H., and D. E. Smith (2009), Non-planar faults: Mechanics of slip and of-fault damage, *Pure Appl. Geophys.*, *166*, 1799–1815, doi:10.1007/s00024-009-0517-y.

Dixon, T. H., M. Miller, F. Farina, H. Wang, and D. Johnson (2000), Present-day motion of the Sierra Nevada block and some tectonic implications for the basin and Range province, North American Cordillera, *Tectonics*, *19*, 1–24.

Dolan, J. F., and B. D. Haravitch (2014), How well do surface slip measurements track slip at depth in large strike-slip earthquakes? The importance of fault structural maturity in controlling on-fault slip versus off-fault surface deformation, *Earth Planet. Sci. Lett.*, *388*, 38–47.

Duan, B. C., and D. D. Oglesby (2005), Multi-cycle dynamics of nonplanar strike slip faults, *J. Geophys. Res.*, *110*, B03304, doi:10.1029/2004JB003298.

Dunham, E. M., D. Belanger, L. Cong, and J. E. Kozdon (2011), Earthquake ruptures with strongly rate-weakening friction and off-fault plasticity, Part 2: Nonplanar faults, *Bull. Seismol. Soc. Am.*, *101*(5), 2308–2322.

Eberhardt-Phillips, D., and A. Michael (1993), Three-dimensional velocity structure, seismicity, and fault structure in the Parkfield region, central California, *J. Geophys. Res.*, *98*, 15,737–15,758.

Elliott, A. J., J. F. Dolan, and D. D. Oglesby (2009), Evidence from coseismic slip gradients for dynamic control on rupture propagation and arrest through stepovers, *J. Geophys. Res.*, *114*, B02313, doi:10.1029/2008JB005969.

Fialko, Y. (2004), Evidence of fluid-filled upper crust from observations of post seismic deformation due to the 1992 M_w 7.3 Landers earthquake, *J. Geophys. Res.*, *109*, B08401, doi:10.1029/2004JB002985.

Fialko, Y., D. Sandwell, D. Agnew, M. Simons, P. Shearer and B. Minster (2002), Deformation on nearby faults induced by the 1999 Hector Mine earthquake, *Science*, *297*, 1858–1862.

Frankel, K. L., J. Dolan, L. A. Owen, P. Ganev, and R. C. Finkel (2011), Spatial and temporal constancy of seismic strain release along an evolving segment of the Pacific North America plate boundary, *Earth Planet. Sci. Lett.*, *304*, 565–576.
Frost, E., J. Dolan, C. G. Sammis, B. R. Hacker, J. Cole, and L. Ratschbacher (2009), Progressive strain localization in a major strike slip fault exhumed from mid seismogenic depths: Structural observations from the Salzach–Ennstal–Mariazell fault system, Austria, *J. Geophys. Res.*, *114*, B04406, doi:10.1029/2008JB005763.
Gold, P. O., M. E. Oskin, A. J. Elliot, A. Hinojosa-Corona, M. H. Taylor, O. Kreylos, and E. Cowgill (2013), Coseismic slip variation assessed from terrestrial lidar scans of the El Mayor–Cucapah surface rupture, *Earth Planet. Sci. Lett.*, *366*, 151–162.
Gutenberg, B., and C. F. Richter (1956), Magnitude and energy of earthquakes, *Ann. Geophys.*, *9*(1), 1–15.
Harris, R. A., and S. M. Day (1993), Correction to "Dynamics of fault interaction: Parallel strike-slip faults," *J. Geophys. Res.*, *98*, 6665, doi:10.1029/93JB00679.
Harris, R. A., R. J. Archulet, and S. Day (1991), Fault steps and the dynamic rupture process: 2-D numerical simulations of a spontaneously propagating shear fracture, *Geophys. Res. Lett.*, *18*, 893–896, doi:10.1029/91GL01061.
Herbert, J. W., M. L. Cooke, M. Oskin, and O. Difo (2014), How much can off-fault deformation contribute to the slip rate discrepancy within the eastern California shear zone?, *Geology*, *42*(1), 71–74, doi:10.1130/G34738.1.
Hollingsworth, J., S. Leprince, F. Ayoub, and J. Avouac (2012), Deformation during the 1975–1984 Krafla rifting crisis, NE Iceland, measured from historical optical imagery, *J. Geophys. Res.*, *117*, B11407, doi:10.1029/2012JB009140.
Hollingsworth, J., S. Leprince, F. Ayoub, and J. P. Avouac (2013), New constraints on dike injection and fault slip during the 1975-84 Krafla rift crisis, NE Iceland, *J. Geophys. Res.*, *118*, 3707–3727, doi:10.1002/jgrb.50223.
Humphreys, E. D., and R. J. Weldon (1994), Deformation across the western United States: A local estimate of Pacific-North America transform deformation, *J. Geophys. Res.*, *99*, 19,975–20,010.
Jachens, R. C., V. E. Langenheim, and J. C. Matti (2002), Relationship of the 1999 Hector Mine and 1992 Landers fault ruptures to offsets on Neogene Faults and distribution of Late Cenozoic Basins in the Eastern California shear zone, *Bull. Seismol. Soc. Am.*, *92*(4), 1592–1605.
Johnson, A. M., R. W. Fleming, and K. M. Cruikshank (1994), Shear zones formed along long, straight traces of fault zones during the 28 June 1992 Landers, California, Earthquake, *Bull. Seismol. Soc. Am.*, *84*(3), 499–510.
Kanamori, H., and D. Anderson (1975), Theoretical basis of some empirical relations in seismology, *Bull. Seismol. Soc. Am.*, *65*(5), 1073–1095.
Kimurah, H., Y. Itoh, and H. Tsutsumi (2004), Quaternary strike-slip crustal deformation around an active fault based on paleomagnetic analysis: A case study of the Enako fault in central Japan, *Earth Planet. Sci. Lett.*, *226*, 321–334, doi:10.1016/j.epsl.2004.08.003.
Klinger, Y., R. Michel, and G. C. P. King (2006), Evidence for an earthquake barrier model from Mw similar to 7.8 Kokoxili (Tibet) earthquake slip distribution, *Earth Planet. Sci. Lett.*, *242*, 354–364.
Konca, O., S. Leprince, J. P. Avouac, and D. V. Helmberger (2010), Rupture process of the 1999 Mw 7.1 Duzce Earthquake from joint analysis of SPOT, GPS, InSAR, strong-motion, and teleseismic data: A supershear rupture with variable rupture velocity, *Bull. Seismol. Soc. Am.*, *100*(1), 267–288, doi:10.1785/0120090072.
Lee, J. J., and R. L. Bruhn (1996), Structural anisotropy of normal fault surfaces, *J. Struct. Geol.*, *18*(8), 1043–1059.
Lemaitre, J., and R. Desmorat (2005), *Engineering Damage Mechanics: Ductile, Creep, Fatigue and Brittle Failures*, 400 pp., Springer, Berlin.
Leprince, S., S. Barbot, F. Ayoub, and J. P. Avouac (2007a), Automatic and precise orthorectification, coregistration, and subpixel correlation of satellite images, application to ground deformation measurements, *IEEE Trans. Geosci. Remote Sens.*, *45*(6), 1529–1558, doi:10.1109/TGRS.2006.888937.
Leprince, S., F. Ayoub, Y. Klinger, and J. P. Avouac (2007b), Co-registration of optically sensed images and correlation (COSI-Corr): An operational methodology for ground deformation measurements, in *International Geoscience Remote Sensing Symposium*, pp. 1943–1946, IEEE, Barcelona, Spain.
Leprince, S., P. Muse, and J. P. Avouac (2008), In-flight CCD distortion calibration for pushbroom satellites based on subpixel correlation, *IEEE Trans. Geosci. Remote Sens.*, *46*(9), 2675–2683, doi:10.1109/TGRS.2008.918649.
Li, Y. G., J. E. Vidale, K. Aki, F. Xu, and T. Burdette (1998), Evidence of shallow fault zone strengthening after the 1992 M7.5 Landers, California, earthquake, *Science*, *279*, 217–219, doi:10.1126/science.279.5348.217.
Lindsey, E. O., V. J. Sahakian, Y. Fialko, Y. Bock, S. Barbot and T. K. Rockwell (2013), Interseismic strain localization in the San Jacinto fault zone, *Pure Appl. Geophys.*, *171*, 2937–2954, doi:10.1007/s00024-013-0753-z.
Liu, J., K. Sieh, and E. Hauksson (2003), A structural interpretation of the aftershock "Cloud" of the 1992 M-w 7.3 Landers earthquake, *Bull. Seismol. Soc. Am.*, *93*(3), 1333–1344, doi:10.1785/0120020060.
Madden, C., D. E. Haddad, J. B. Salisbury, O. Zielke, J. R. Arrowsmith, R. J. Weldon, and J. Colunga (2013), Appendix R—Compilation of slip-in-the-last-event data and analysis of last event, repeated slip, and average displacement for recent and prehistoric ruptures, *U.S. Geol. Surv. Open File Rep.*, *1165*, 65 pp.
Mai, P. M., and G. C. Beroza (2002), A spatial random field model to characterize complexity in earthquake slip, *J. Geophys. Res.*, *107*, 2308, doi:10.1029/2001/JB000588.
Mamada, Y., Y. Kuwahara, H. Ito, and H. Takenaka (2004), Discontinuity of the Mozumi-Sukenobu fault low-velocity zone, central Japan, inferred from 3-D finite-difference simulation of fault zone waves excited by explosive sources, *Tectonophysics*, *378*, 209–222, doi:10.1016/j.tecto.2003.09.008.
Mandelbrot, B. B. (1983), *The Fractal Geometry of Nature*, 3rd ed., W. H. Freeman, N. Y.
Martel, S. J., D. D. Pollard, and P. Segall (1988), Development of simple fault zones in granitic rock, Mount Abbot Quadrangle, Sierra Nevada, California, *Geol. Soc. Am. Bull.*, *100*, 1451–1465.
McGill, S. F., and C. M. Rubin (1999), Surficial slip distribution on the central Emerson fault during the June 28, 1992, Landers earthquake, California, *J. Geophys. Res.*, *104*, 4811–4833.
McGuire, J., and Y. Ben-Zion (2005), High-resolution imaging of the Bear Valley section of the San Andreas fault at seismogenic depths with fault-zone head waves and relocated seismicity, *Geophys. J. Int.*, *163*, 152–164, doi:10.1111/j.1365-246X.2005.02703.x.
Michel, R., and J. P. Avouac (2006), Coseismic surface deformation from air photos: The Kickapoo step over in the 1992 Landers rupture, *J. Geophys. Res.*, *111*, B03408, doi:10.1029/2005JB003776.
Miller, D. M., and J. C. Yount (2002), Late Cenozoic tectonic evolution of the north-central Mojave Desert inferred from fault history and physiographic evolution of the Fort Irwin area, California, *Mem. Geol. Soc. Am.*, *195*, 173–197.
Milliner, C. W., J. Hollingsworth, J. F. Dolan, S. Leprince, F. Ayoub, and J. P. Avouac (2012), Analysis of the shallow slip deficit using sub-pixel image correlation: Examples from various large continental strike-slip earthquakes, Abstract T13D-2652 presented at 2012 Fall Meeting, AGU, San Francisco, Calif., 3–7 Dec.
Nelson, M. R., and C. H. Jones (1987), Paleomagnetism and crustal rotations along a shear zone, Las Vegas Range, southern Nevada, *Tectonics*, *6*, 13–33, doi:10.1029/TC006i001p00013.

Nissen, E., T. Maruyama, R. J. Arrowsmith, J. R. Elliott, A. K. Krishnan, M. E. Oskin, and S. Saripalli (2014), Coseismic fault zone deformation revealed with differential lidar: Examples from Japanese Mw~7 intraplate earthquakes, *Earth Planet. Sci. Lett.*, *405*, 244–256, doi: 10.1016/j.epsl.2014.08.031.

Oglesby, D. (2008), Rupture termination and jump on parallel offset faults, *Bull. Seismol. Soc. Am.*, *98*, 440–447.

Okubo, P. G., and K. Aki (1987), Fractal geometry in the San Andreas fault system, *J. Geophys. Res.*, *92*, 345–355.

Oskin, M., L. Perg, D. Blumentritt, S. Mukhopadhyay, and A. Iriondo (2007), Slip rate of the Calico fault: Implications for geologic versus geodetic discrepancy in the Eastern Califonia shear zone, *J. Geophys. Res.*, *112*, B03402, doi:10.1029/2006JB004451.

Oskin, M., L. Perg, E. Shelef, M. Strane, E. Gurney, B. Singer, and X. Zhang (2008), Elevated shear zone loading rate during an earthquake cluster in eastern California, *Geology*, *36*(6), 507–510.

Oskin, M. E., et al. (2012), Near-field deformation from the El Mayor–Cucapah Earthquake revealed by differential LIDAR, *Science*, *335*, 702–705.

Peltzer, G., P. Rosen, F. Rogez, and K. Hudnut (1998), Poroelastic rebound along the Landers 1992 earthquake surface rupture, *J. Geophys. Res.*, *103*, 30,131–30,145.

Peng, Z., Y. Ben-Zion, A. J. Michael, and L. Zhu (2003), Quantitative analysis of fault zone waves in the rupture zone of the Landers, 1992, California earthquake: Evidence for a shallow trapping structure, *Geophys. J. Int.*, *155*, 1021–1041, doi:10.1111/j.1365-246X.2003.02109.

Petersen, M. D., T. E. Dawson, R. Chen, T. Cao, C. J. Wills, D. P. Schwartz, and A. D. Frankel (2011), Fault displacement hazard for strike-slip faults, *Bull. Seismol. Soc. Am.*, *101*(2), 805–825, doi:10.1785/0120100035.

Power, W. L., and T. E. Tullis (1995), Review of the fractal character of natural fault surfaces with implications for friction and the evolution of fault zones, in *Fractals in the Earth Sciences*, edited by C. C. Barton, and P. R. L. Pointe, chap. 5, pp. 89–105, Plenum, N. Y.

Power, W. L., T. E. Tullis, and J. D. Weeks (1988), Roughness and wear during brittle faulting, *J. Geophys. Res.*, *93*, 15,268–15,278.

Powers, P. M., and T. H. Jordan (2010), Distribution of seismicity across strike-slip faults in California, *J. Geophys. Res.*, *115*, B05305, doi: 10.1029/2008JB006234.

Quigley, M., R. Van Dissen, N. Litchfield, P. Villamor, B. Duffy, D. Barrell, K. Furlong, T. Stahl, E. Bilderback, and D. Noble (2012), Surface rupture during the 2010 M(w) 7.1 Darfield (Canterbury) earthquake: Implications for fault rupture dynamics and seismic-hazard analysis, *Geology*, *40*, 55–58.

Renard, F., C. Voisin, D. Marsan, and J. Schmittbuhl (2006), High resolution 3D laser scanner measurements of a strike-slip fault quantify its morphological anisotropy at all scales, *Geophys. Res. Lett.*, *33*, L04305, doi:10.1029/2005GL025038.

Robertson, M. C., C. G. Sammis, M. Sahimi, and A. Martin (1995), The 3-D spatial distribution of earthquakes in southern California with a percolation theory interpretation, *J. Geophys. Res.*, *100*, 609–620.

Rockwell, T. K., and Y. Klinger (2013), Surface rupture and slip distribution of the 1940 Imperial Valley Earthquake, Imperial Fault, Southern California: Implications for rupture segmentation and dynamics, *Bull. Seismol. Soc. Am.*, *103*(2A), 629–640, doi:10.1785/0120120192.

Rockwell, T. K., S. Lindvall, T. Dawson, R. Langridge, W. R. Lettis, and Y. Klinger (2002), Lateral offsets on surveyed cultural features resulting from the 1999 Izmit and Düzce Earthquakes, Turkey, *Bull. Seismol. Soc. Am.*, *92*, 79–94, doi:10.1785/0120000809.

Sagy, A., E. E. Brodsky, and G. J. Axen (2007), Evolution of fault-surface roughness with slip, *Geology*, *35*(3), 283–286, doi:10.1130/G23235A.1.

Salisbury, J. B., J. R. Arrowsmith, T. K. Rockwell, D. E. Haddad, O. Zielke, and C. Madugo (2012), Subjectivity of LiDAR-based offset measurements: Results from a public online survey, Abstract T13D-2634 presented at 2012 Fall Meeting, AGU, San Fransico, Calif.

Sammis, C. G., A. J. Rosakis, and H. S. Bhat (2009), Effects of Off-fault damage on earthquake rupture propagation: Experimental studies, *Pure Appl. Geophys.*, *166*, 1629–1648.

Sauber, J., W. Thatcher, S. C. Solomon, and M. Lisowski (1994), Geodetic slip rate for the eastern California shear zone and the recurrence time of Mojave Desert earthquakes, *Nature*, *367*, 264–266, doi:10.1038/367264a0.

Scharer, K. M., J. B. Salisbury, J. R. Arrowsmith, and T. K. Rockwell (2014), Southern San Andreas Fault Evaluation field activity: Approaches to measuring small geomorphic offsets—Challenges and recommendations for active fault studies, *Seismol. Res. Lett.*, *85*, 68–76.

Schwartz, D. P., and K. J. Coppersmith (1984), Fault behavior and characteristic earthquakes' examples from the Wasatch and San Andreas Fault Zones, *J. Geophys. Res.*, *89*, 5681–5698.

Segall, P., and D. D. Pollard (1980), Mechanics of discontinuous faults, *J. Geophys. Res.*, *85*, 4337–4350.

Shelef, E., and M. Oskin (2010), Deformation processes adjacent to active faults: Examples from eastern California, *J. Geophys. Res.*, *115*, B05308, doi:10.1029/2009JB006289.

Sibson, R. H. (2003), Thickness of the seismic slip zone, *Bull. Seismol. Soc. Am.*, *93*, 1169–1178.

Sieh, K., et al. (1993), Near-field investigations of the Landers earthquake sequence, April to July 1992, *Science*, *260*, 171–176.

Simons, M., Y. Fialko and L. Rivera (2002), Co-seismic static deformation from the 1999 M_w7.1 Hector Mine, California, earthquake, as inferred from InSAR and GPS observations, *Bull. Seismol. Soc. Am.*, *92*, 1390–1402.

Spotila, J. A., and K. Sieh (1995), Geologic investigations of a "slip gap" in the surficial ruptures of the 1992 Landers earthquake, southern California, *J. Geophys. Res.*, *100*, 543–559.

Teran, O. J., et al. (2011), Structural Controls on the Surface Rupture Associated with the Mw7.2 El Mayor–Cucapah Earthquake of 4 April 2010: A Comparative Analysis of Scarp Array Kinematics, Orientation, Lithology and Width. Poster Abstract A-118 presented at 2011 Southern California Earthquake Center Annual Meeting, Palm Springs, Calif., 11–14 Sep.

Thomson, D. J. (1982), Spectrum estimation and harmonic analysis, *Proc. IEEE*, *70*, 1055–1096.

Treiman, J. A., K. J. Kendrick, W. A. Bryant, T. K. Rockwell and S. F. McGill (2002), Primary surface rupture associated with the Mw 7.1 16 October 1999 Hector Mine earthquake, San Bernardino County, California, *Bull. Seismol. Soc. Am.*, *92*, 1171–1191, doi:10.1785/0120000923.

Turcotte, D. L. (1997), *Fractals and Chaos in Geology and Geophysics*, 2nd ed., 398 p., Cambridge Univ. Press, Cambridge, U. K.

Van Dissen, R., et al. (2011), Surface rupture displacement on the Greendale Fault during the M (sub w) 7.1 Darfield (Canterbury) earthquake, New Zealand, and its impact on man-made structures, in *Proceedings Ninth Pacific Conference on Earthquake Engineering*, *Building an Earthquake-Resilient Society*, *Pap. 186*, 8 pp., N. Z. Soc. for Earthquake Eng., Auckland.

Vermilye, J. M., and C. H. Scholz (1998), The process zone: A microstructural view of fault growth, *J. Geophys. Res.*, *103*, 12,223–12,237, doi: 10.1029/98JB00957.

Wald, D. J., and T. H. Heaton (1994), Spatial and temporal distribution of slip for the 1992 Landers, California, Earthquake, *Bull. Seismol. Soc. Am.*, *84*, 668–691.

Wesnousky, S. G. (1988), Seismological and structural evolution of strike-slip faults, *Nature*, *335*, 340–343.

Wesnousky, S. G. (1990), Seismicity as a function of cumulative geologic offset: Some observations from Southern California, *Bull. Seismol. Soc. Am.*, *80*, 1374–1381.

Wesnousky, S. G. (2006), Predicting the endpoints of earthquake ruptures, *Nature*, *444*, 358–360, doi:10.1038/nature0525.

Wesnousky, S. G. (2008), Displacement and geometrical characteristics of earthquake surface ruptures: Issues and implications for seismic-hazard analysis and the process of earthquake rupture, *Bull. Seismol. Soc. Am.*, *98*, 1609–1632.

Yamashita, T. (2000), Generation of microcracks by dynamic shear rupture and its effects on rupture growth and elastic wave radiation, *Geophys. J. Int.*, *143*, 395–406, doi:10.1046/j.1365-246X.2000.01238.x.

Zachariasen, J., and K. Sieh (1995), The transfer of slip between two en-echelon strike-slip faults: A case study from the 1992 Landers earthquake southern California, *J. Geophys. Res.*, *100*, 15,281–15,301.

Zielke, O., J. R. Arrowsmith, L. G. Ludwig, and S. O. Akciz (2012), High-resolution topography-derived offsets along the 1857 Fort Tejon Earthquake Rupture Trace, San Andreas Fault, *Bull. Seismol. Soc. Am.*, *102*(3), 1135–1154, doi:10.1785/0120110230.

Zinke, R., J. Hollingsworth, and J. F. Dolan (2014), Surface slip and off-fault deformation patterns in the 2013 MW 7.7 Balochistan, Pakistan earthquake: Implications for controls on the distribution of near-surface coseismic slip, *Geochem. Geophys. Geosyst.*, *15*, 5034–5050, doi:10.1002/2014GC005538.